JACS Au
AN OPEN ACCESS JOURNAL OF THE AMERICAN CHEMICAL SOCIETY

pubs.acs.org/jacsau

Article

Can Second Coordination Sphere and Long-Range Interactions Modulate Hydrogen Atom Transfer in a Non-Heme Fe(II)-Dependent Histone Demethylase?

Shobhit S. Chaturvedi, Simahudeen Bathir Jaber Sathik Rifayee, Sodiq O. Waheed, Jon Wildey, Cait Warner, Christopher J. Schofield, Tatyana G. Karabencheva-Christova, and Christo Z. Christov*

Cite This: *JACS Au* 2022, 2, 2169–2186

Read Online

ACCESS | Metrics & More | Article Recommendations | Supporting Information

ABSTRACT: Fe(II)-dependent oxygenases employ hydrogen atom transfer (HAT) to produce a myriad of products. Understanding how such enzymes use dynamic processes beyond the immediate vicinity of the active site to control the selectivity and efficiency of HAT is important for metalloenzyme engineering; however, obtaining such knowledge by experiments is challenging. This study develops a computational framework for identifying second coordination sphere (SCS) and especially long-range (LR) residues relevant for catalysis through dynamic cross-correlation analysis (DCCA) using the human histone demethylase PHF8 (KDM7B) as a model oxygenase. Furthermore, the study explores the mechanistic pathways of influence of the SCS and LR residues on the HAT reaction. To demonstrate the plausibility of the approach, we investigated the effect of a PHF8 F279S clinical mutation associated with X-linked intellectual disability, which has been experimentally shown to ablate PHF8-catalyzed demethylation. In agreement, the molecular dynamics (MD) and quantum mechanics/molecular mechanics (QM/MM) studies showed a change in the $H3_{1-14}$K9me2 substrate orientation and an increased HAT barrier. We systematically analyzed the pathways by which the identified SCS and LR residues may influence HAT by exploring changes in H3K9me2 substrate orientation, interdomain correlated motions, HAT transition state stabilization, reaction energetics, electron transfer mechanism, and alterations in the intrinsic electric field of PHF8. Importantly, SCS and LR variations decrease key motions of $\alpha9-\alpha12$ of the JmjC domain toward the Fe(IV)-center that are associated with tighter binding of the $H3_{1-14}$K9me2 substrate. SCS and LR residues alter the intrinsic electric field of the enzyme along the reaction coordinate and change the individual energetic contributions of residues toward TS stabilization. The overall results suggest that DCCA can indeed identify non-active-site residues relevant for catalysis. The substitutions of such dynamically correlated residues might be used as a tool to tune HAT in non-heme Fe(II)- and 2OG-dependent enzymes.

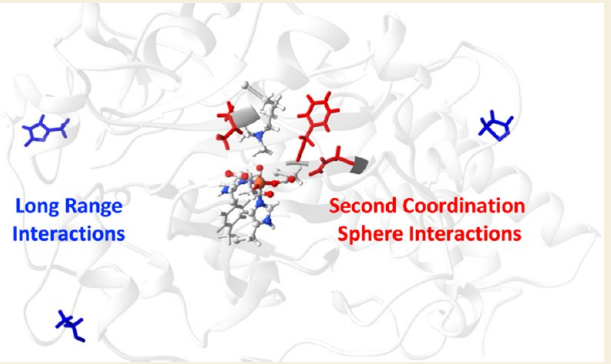

KEYWORDS: *hydrogen atom transfer, non-heme Fe(II)/2OG-dependent enzymes, conformational dynamics, second coordination sphere, long-range interactions*

INTRODUCTION

Hydrogen atom transfer (HAT) is fundamental to many important chemical and biological reactions.[1] Many heme and non-heme enzymes and iron-containing model complexes employ HAT to selectively activate C−H bonds, producing an incredibly diverse set of products.[2−6] The factors influencing HAT reactions have been extensively explored, including by studying isotope effects,[7] the spin states of the substrate and oxidizing species,[8] and the roles of tunneling effects.[9] Many HAT reactions follow the Evans and Polanyi correlation[10] and satisfy the Marcus theory;[11] however, there are exceptions described in the literature.[12] The effect of ordering the spin state of the transition state (TS) structure, the TS stereoelectronics, and the first ligand sphere on HAT have been investigated in heme and non-heme iron synthetic model complexes.[9] Quantum mechanics (QM) and quantum mechanics/molecular mechanics (QM/MM) methods have been extensively used to define HAT molecular orbital (MO) mechanisms in both model compounds and enzymes.[13−18] However, enzyme-catalyzed HAT reactions are complicated by factors including the: (i) effects of second coordination sphere

Received: June 9, 2022
Revised: July 25, 2022
Accepted: August 1, 2022
Published: August 18, 2022

https://doi.org/10.1021/jacsau.2c00345
JACS Au 2022, 2, 2169−2186

(SCS) residues noncovalently interacting with the active site and the substrate; (ii) interactions between the active site and long-range (LR) residues in remote areas; (iii) conformational motions of the enzyme and substrate during catalysis; (iv) effects of the protein's intrinsic electric field on HAT. These factors have the potential to modulate the efficiency of HAT, including by altering its energetics, molecular orbital mechanism, and interaction energies that stabilize the TS. Despite intensive studies, the nature and extent of the influence of the overall protein structure on the HAT reactions in enzymes remain poorly understood. This knowledge is important in structure-guided efforts to modulate and improve the selectivity and efficiency of enzyme-catalyzed HAT reactions.

Non-heme Fe(II)/2-oxoglutarate (2OG) oxygenases, including histone demethylases (JmjC KDMs), DNA demethylases, TET enzymes, and ethylene-forming enzymes (EFE) perform HAT as a part of their reactions.[19] Earlier studies have demonstrated that substitutions in both the SCS and LR regions can significantly affect their catalytic activity;[20−22] such substitutions are also linked to disease.[22,23] Importantly, the ability of SCS residues to induce fast motions has been demonstrated by experimental work, including on a penicillin-forming oxidase, which is structurally and mechanistically related to the 2OG oxygenases.[24−26] Further, an SCS substitution of lysine (K241) to alanine in the 2OG-dependent JmjC KDM4A has been shown to ablate demethylation activity.[27] A computational study explored the effects of K241A, Y177A, and N290A variations in KDM4A and demonstrated that in these variants, the histone substrate (H3K4me3) adopts a nonproductive conformation;[28] these results are in agreement with experimental studies for K241A.[28] Hu et al. have reported that TET2 variants Y1902A, N1387A, S1290A-Y1295A, and K1299E-S1303N manifest substantially decreased activities, despite some variants being located far away from the active site Fe.[22] Computational study on these variants implies that the variants have an increased HAT energy barrier through alterations in the intrinsic electric field of TET2 along the reaction coordinate and changed substrate orientation and binding.[29] Mutagenesis studies on the ethylene-forming enzyme (EFE) indicate that replacement of residues both in the active site (R171A) and at the enzyme surface (E215A) can severely affect catalysis.[21] Computational studies of EFE R171A further revealed its structural and mechanistic effect on the 2OG binding in agreement with the experimental data.[30] Intriguingly, substitutions in non-heme enzymes both in the SCS and at LR can influence the coordination state of the active site (as exemplified in studies on factor inhibiting hypoxia-inducible factor (FIH))[31] and can improve nonstandard reaction modes (e.g., the nitrene-transfer reaction of an EFE variant).[32] In other enzyme classes, e.g., dihydrofolate reductase (DHFR), variations of loop residues can increase its affinity for the cofactor while decreasing its affinity for folate such that the mechanism is altered at key stages of catalysis.[33] Thus, both experimental and computational studies indicate that SCS and LR interactions play important roles in catalysis by Fe(II) oxygenases.

The ability of SCS and LR residues to alter enzyme catalysis makes them an excellent target for engineering. Experimental methods such as directed evolution have been employed to improve and/or alter catalytic properties of enzymes,[34] as have computational methods including ROSETTA,[35−37] shortest path sampling,[38] and molecular dynamics (MD) simulations.[39,40] However, identifying residues at LR from the active site relevant for catalysis remains challenging, and experimental approaches, e.g., employing X-ray free electron laser-based analyses to study correlated motions during specific steps in catalysis by oxygenases, are demanding and expensive.[26,41] Recent studies demonstrated that electrostatic perturbations could be a promising tool to modulate the rate and specificity of chemical reactions.[42−44] Computational methods thus have an important role in studying factors away from the active site that regulates the kinetics of individual steps in oxygenase catalysis.[28,29,45]

To investigate the potential effect of variations in the SCS and LR areas on the HAT step of an oxygenase, we performed a computational study on human histone demethylase PHF8 (KDM7B) variants. PHF8 is a human non-heme Fe(II)/2OG-dependent oxygenase that catalyzes the demethylation of di-/mono-methylated lysine-9 of the N-terminal tail of human histone H3 ($H3_{1-14}$K9me2/1).[46,47] Alterations in the structure and, likely, activity of PHF8 correlate with X-linked intellectual disability[23,48] and various types of cancer.[49−51] PHF8 is a multidomain enzyme that contains a catalytic (JmjC) domain, a reader (PHD) domain, and a linker region connecting the two domains. The catalytic JmjC domain has the non-heme Fe(II) center where the metal is ligated by a facial triad of residues—His_{247}-X-Asp_{249}-Y-His_{319}; the co-substrate 2OG and dioxygen coordinate the Fe during catalysis. The PHD domain contains two zinc-centers and binds to tri-methylated lysine4 of H3 (H3K4me3). The binding of H3K4me3 to the PHD domain orders the catalytic JmjC domain for demethylation at $H3_{1-14}$K9me2, in a manner related to the nature of the linker region.[46,52] Similar to other 2OG-dependent histone lysine demethylases (KDMs),[19,53] the proposed mechanism for PHF8 involves dioxygen activation to give an enzyme·Fe(III)·OO^{-}·2OG·substrate complex that reacts to form a ferryl (Fe(IV)═O) concomitant with decarboxylation of 2OG to succinate and CO_2 (Scheme S1). The ferryl intermediate exploits HAT to abstract a hydrogen from the lysine *N*-methyl group of $H3_{1-14}$K9me2 of the histone substrate (Scheme 1),

Scheme 1. HAT from a Methyl Group of H3K9me2 Substrate in PHF8

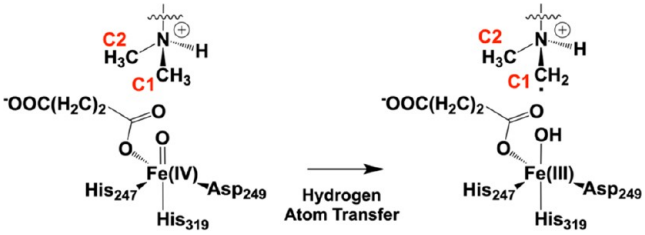

yielding a hydroxylated product through a rebound mechanism. The hydroxylated *N*-methyl group of $H3_{1-14}$K9me2 histone substrate then decomposes to form formaldehyde and the demethylated lysine. The HAT mechanism in PHF8 has been explored; importantly, SCS residues stabilizing the HAT TS structure have been identified.[45] The prior experimental and modeling studies on the WT PHF8[45] mechanism make it an excellent system for investigating the effects of variations in the SCS and LR areas on HAT.

In this study, we aimed to develop a framework for identifying SCS residues and specifically catalytically relevant

https://doi.org/10.1021/jacsau.2c00345
JACS Au 2022, 2, 2169−2186

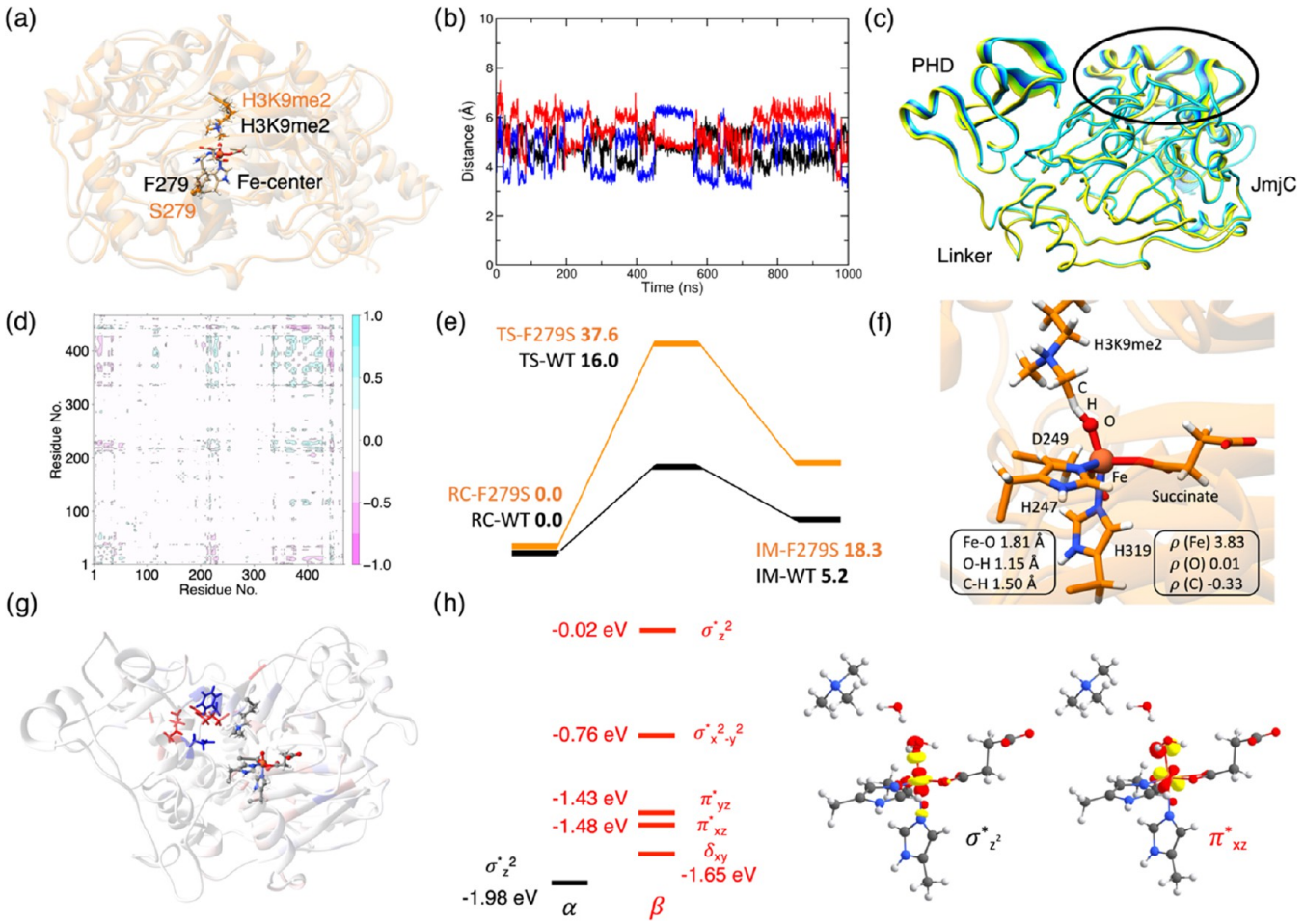

Figure 1. Effects of PHF8 F279S clinical variant on the HAT reaction. (a) Superimposed MD structure of the F279S variant (orange) on the WT MD structure (tan). (b) Distance between the ferryl oxygen and first methyl carbon (C1, black), second methyl carbon (C2, blue), and amine hydrogen (red) of the H3K9me2 in the F279S variant. (c) Principal component analysis (PCA) showing the direction of motions of the most flexible regions in the PHF8 F279S variant. The color gradient from yellow to blue indicates the direction of motion. (d) Differential DCCA showing correlated motions in the F279S variant with respect to WT PHF8. (e) Potential energy surface (PES) for HAT in the F279S variant. (f) The QM/MM-optimized geometry of **TS-F279S**. (g) Primary residues stabilizing (blue) and destabilizing (red) the **TS-F279S** with respect to the **RC-F279S**. (h) FMOs and their energies for HAT reaction in the F279S variant.

LR residues through analysis of dynamics cross-correlation analysis (DCCA). Furthermore, we aimed to delineate the multiple mechanistic pathways of influence of the SCS and LR residues on the HAT reaction such as effects on the activation energy, molecular orbital mechanism, structures and flexibilities of the reactant complex (RC) and TS, interdomain correlated motions and altering the intrinsic electric field of the enzyme. Such type of study requires systematic and comprehensive analysis, and therefore we focused on a single and well-studied reaction step −HAT,[45] the rate-limiting step in chemical steps catalyzed by WT PHF8. We selected three SCS residues that are critical in stabilizing the orientation of the H3K9me2 substrate and Fe-center for the HAT in PHF8.[45] Additionally, we identified three LR residues from different domains of PHF8—the PHD, the linker, and the JmjC domain that might be relevant for HAT reaction. To validate the impact of identified SCS and LR residues on the HAT step for PHF8, we substituted all of the identified SCS and LR residues with alanine. The computational methodology used for the purpose was validated for an experimentally verified F279S variant of PHF8 that affects its activity.[48] The applied MD and QM/MM methods have also been shown to correlate with experimental results of mutant forms of other 2OG-dependent enzymes, i.e., KDM4A, TET2, and EFE.[28−30] The results inform on the potential of the SCS and LR residues to modulate the activation barrier for HAT, product stabilization, and the molecular orbital mechanism. The methodology applied in this study for identifying LR residues relevant to catalysis through DCCA in the case of PHF8 will be applicable to related Fe(II)/2OG oxygenases.

METHODS

A crystal structure of the PHF8 $H3_{1-14}$ histone substrate complex (PDB ID: 3KV4) was used for modeling.[46] The starting PHF8·Fe(IV)═O·succinate·$H3_{1-14}$K9me2 structure for the PHF8 clinical variant and the SCS and LR variant simulations was prepared similarly to the procedure used for the reported WT PHF8 calculations.[45] The MD and QM/MM simulation parameters were maintained to enable rigorous comparison.[45] MD simulations were performed with the AMBER 16 program.[54] ChemShell[55] was used for QM/MM calculations, with Turbomole[56] being used for the QM part and DL_POLY[57] for the MM part. The Fe, succinate, oxo, first sphere coordinating residues (H247, D249, H319), K9me2, and two water molecules were included in the QM region (Figure S1). The unrestricted B3LYP functional with def2-SVP basis set [QM(B1)/

https://doi.org/10.1021/jacsau.2c00345
JACS Au 2022, 2, 2169−2186

MM] was used for geometry optimization and frequency calculations. Improved single-point energy corrections were done using a large all-electron basis set def2-TZVP [QM(B2)/MM] with B3LYP functional. The zero-point energy and D3 dispersion corrections were applied to all geometries, and the final energies are reported as [QM(B2 + ZPE + D3)/MM] energies. A detailed method description is provided in Supporting Information (SI).

RESULTS AND DISCUSSION

Exploring the Effects of Clinical F279S Variant on HAT and Validation of Methods

An F279S variation in PHF8 is linked with X-linked intellectual disability[23,48] and has been shown experimentally to abolish PHF8-catalyzed demethylation of H3K9me2.[48] The DCCA of the Fe(IV)=O·succinate·$H3_{1-14}$K9me2 complex of the WT PHF8[45] indicates that residue F279 participates in correlated motions with the Fe(IV) (with a correlation coefficient of 0.22, indicating F279 has correlated motions with Fe in 22% of the MD trajectory), the ferryl oxygen (0.17), Fe-ligating residues—H247 (0.48), H319 (0.43), D249 (0.19) and H3K9me2 of the substrate (0.11). This result demonstrates that DCCA is a reliable tool for identifying residues that can potentially affect catalysis. To further demonstrate the plausibility of the computational approach applied in this study, we investigated the effects of F279S PHF8 variation on the $H3_{1-14}$K9me2 substrate binding and HAT reaction mechanism (Figure 1).

In contrast to WT PHF8,[45] the dynamics of the F279S variant at the ferryl intermediate stage show no clear preference between the two methyl groups of H3K9me2 (Figure 1b). The average distance between both the two methyl carbons (C1 and C2) to the ferryl oxygen is 4.7 Å compared to 4.9 and 4.4 Å in WT PHF8,[45] respectively. Hydrogen bonding interactions of the Fe(IV)-coordinating residues and the H3K9me2 show minor differences compared to the WT PHF8[45] (Table S1). The PCA of the F279S Fe(IV)=O·succinate·$H3_{1-14}$K9me2 complex indicates the direction of motion for α9 to α12 is more toward the PHD than toward the Fe-center as in the WT PHF8 (Figure 1c). However, free energy calculation using molecular mechanics with generalised Born and surface area solvation (MMGBSA) indicates that the overall binding of the H3 histone substrate with PHF8 is not affected by the F279S substitution and has a value of −140.8 ± 12.5 kcal/mol with respect to −139.0 ± 14.1 kcal/mol in WT PHF8.[45] Consistent with the results of PCA, the differential DCCA in respect to the WT PHF8 shows increased anticorrelated motion between the PHD and the α9 to α12 regions of JmjC domain (Figure 1d). Together the results indicate that the F279S variant affects the orientation of the side chain of substrate's K9me2 with respect to the Fe-center and disrupts the motion between α9 to α12 regions of the JmjC domain by inducing increased correlated motions of both α9 to α12 regions with the PHD domain.

We investigated whether the methods used in the manuscript can predict the ablation of HAT reactivity in the PHF8 F279S variant, as observed in experiments.[48] A snapshot from well-equilibrated MD trajectories (>500 ns) representing an average MD distance between the ferryl oxygen atom and the methyl carbon (O−C1), and with an average angle between the Fe(IV), the ferryl oxygen, and the substrate carbon (∠Fe−O−C1), was used to select an initial structure for QM/MM calculations (Table S2). The QM/MM-optimized RC of F279S (**RC-F279S**) shows an increased distance to 3.82 Å between the ferryl oxygen and hydrogen of the C1 methyl of K9me2 compared to a distance of 2.26 Å in **RC-WT**. An increased distance between the ferryl oxygen and the substrate has been demonstrated to increase the HAT energy barrier in another 2OG-dependent histone lysine demethylase, KDM4A.[28] Indeed, QM/MM potential energy surface starting from **RC-F279S** show the energy required to cross the **TS-F279S** is 37.6 kcal/mol (Figure 1e) compared to 16.0 kcal/mol for WT PHF8. The Fe(III)−OH product (**IM-F279S**) formed in the reaction is endothermic by 18.3 kcal/mol compared to 5.2 kcal/mol in WT PHF8. Spin density analysis of the **TS-F279S** shows a spin density of 3.83 on Fe, 0.01 on ferryl oxygen, and −0.33 on the substrate carbon indicating an α electron is transferred from the substrate methyl C−H to the Fe.

We investigated the factors influencing the HAT reaction in WT PHF8 and how they evaluate in the F279S variant. We applied energy decomposition analysis (EDA)[58,59] on the **TS-WT** to extract individual energetic contributions of residues involved in the TS stabilization in the WT enzyme (Figures S2 and S3) and the clinical F279S variant (Figures 1g and S4). EDA of WT PHF8 indicates H3R8 and Y234 as residues important in stabilizing the **TS-WT**, by −0.6 and −0.3 kcal/mol, respectively. Residues L169 and T244 destabilize the **TS-WT** by 0.4 and 0.3 kcal/mol, respectively. The individual energetic contribution of other PHF8 and $H3_{1-14}$K9me2 substrate residues toward TS stabilization is given in Figure S3. The EDA of the F279S variant indicates that E350 (−3.0 kcal/mol) and F359 (−2.4) are the primary residues stabilizing the **TS-F279S** with respect to **RC-F279S**, while K351 (1.2) and R360 (1.1) are the primary TS destabilizing residues. Thus, the results indicate that the F279S variant affects the individual energetic contributions of residues involved in stabilizing and destabilizing the HAT TS. We further compared the intrinsic electric field in WT PHF8 and F279S variant along the Fe=O bond to explore if the F279S influences the intrinsic electric field of PHF8 for HAT. The QM/MM-optimized **RC-WT** showed an intrinsic electric field of −0.0272 au along the Fe=O bond direction, while the intrinsic electric field in **RC-F279S** is reduced to −0.0265 au.

Spectroscopic and computational studies on several HS non-heme Fe(II) enzymes indicate that the two frontier MOs—$\sigma^*_{z^2}$ and $\pi^*_{xz/yz}$ can act as acceptor orbitals in HAT.[13,14] However, our MO analysis on five HAT reaction path calculations of the WT PHF8 indicated that in all of them, the $\sigma^*_{z^2}$ orbital is the electron acceptor orbital.[45] Molecular orbital analysis of the **RC-WT** shows that $\sigma^*_{z^2}$ is the lowest unoccupied molecular orbital (LUMO) and the π^*_{xz} is higher in energy by 0.12 eV (2.76 kcal/mol), and therefore $\sigma^*_{z^2}$ is the preferred electron acceptor orbital in WT PHF8 (Figure S5). A similar molecular orbital analysis of the **RC-F279S** variant indicates that $\sigma^*_{z^2}$ is still the LUMO in the F279S variant. However, the energy difference between the two acceptor orbitals $\sigma^*_{z^2}$ and the π^*_{xz} is increased to 0.33 eV (7.61 kcal/mol) (Figure 1h), indicating that the F279S variant influences the energy difference between the FMOs of the HAT reaction. The results from the MD of the F279S variant demonstrate that DCCA can indeed provide validated suggestions for identifying catalytically relevant SCS and LR residues. The high energy requirement for HAT reaction obtained from QM/MM calculations of PHF8 F279S variant agrees with experimental studies[48] and provides a mechanistic explanation for the loss of activity in F279S PHF8. The MD and QM/MM

https://doi.org/10.1021/jacsau.2c00345
JACS Au 2022, 2, 2169−2186

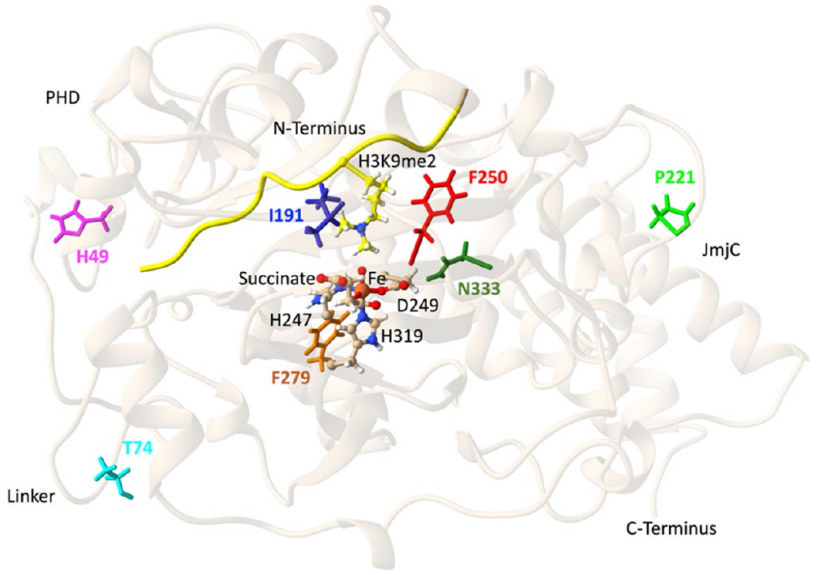

Figure 2. Locations of clinically observed PHF8 F279 variant, SCS residues (I191, F250, N333), and LR residues (P221, H49, and T74) that are the subject of our work with respect to the Fe(IV)═O·succinate·$H3_{1-14}$K9me2 complex. The $H3_{1-14}$K9me2 substrate is highlighted in yellow.

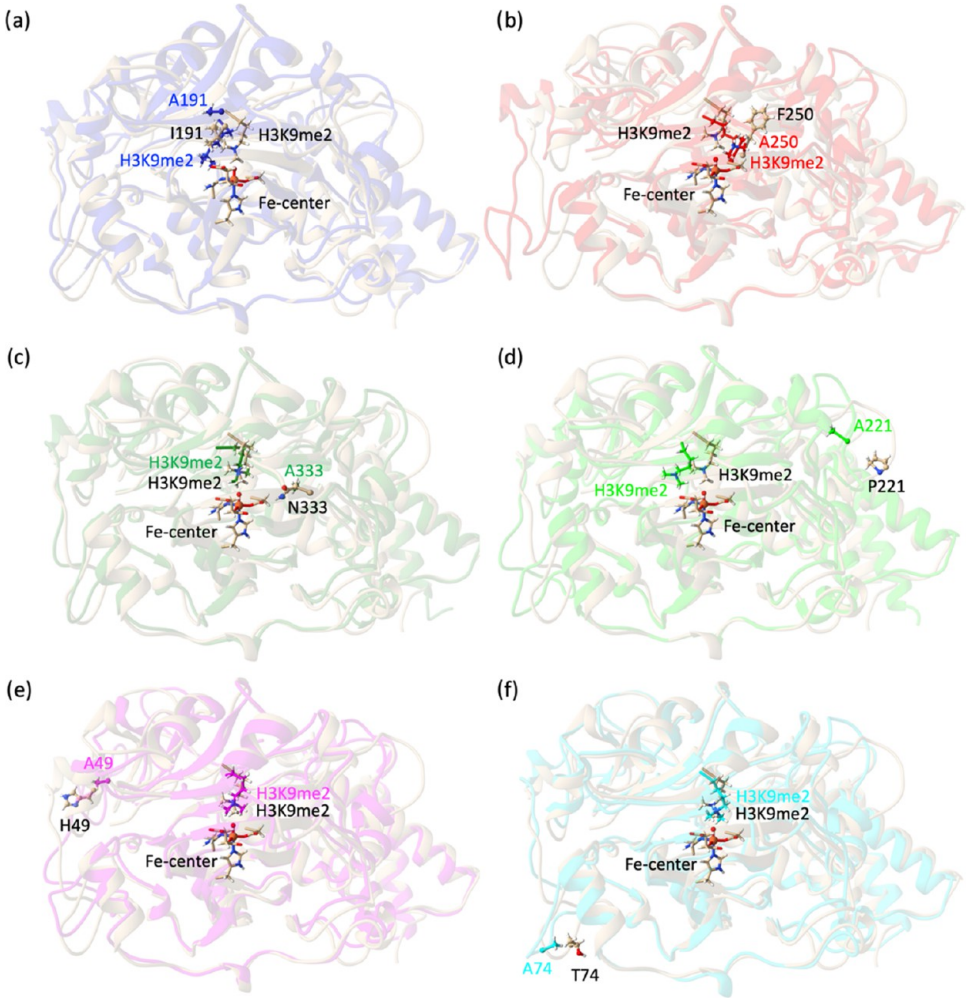

Figure 3. Superimposed MD structures of SCS variants: (a) I191A, (b) F250A, and (c) N333A, and LR variants: (d) P221A, (e) H49A, and (f) T74A on the WT MD structure (tan) highlighting changes in H3K9me2 substrate orientation.

methods applied in this study have also been validated to reproduce the effects of multiple mutations in other Fe(II)/2OG-dependent enzymes, i.e., KDM4A, TET2, and EFE (a detailed description is given in the SI).[28−30]

https://doi.org/10.1021/jacsau.2c00345
JACS Au 2022, 2, 2169−2186

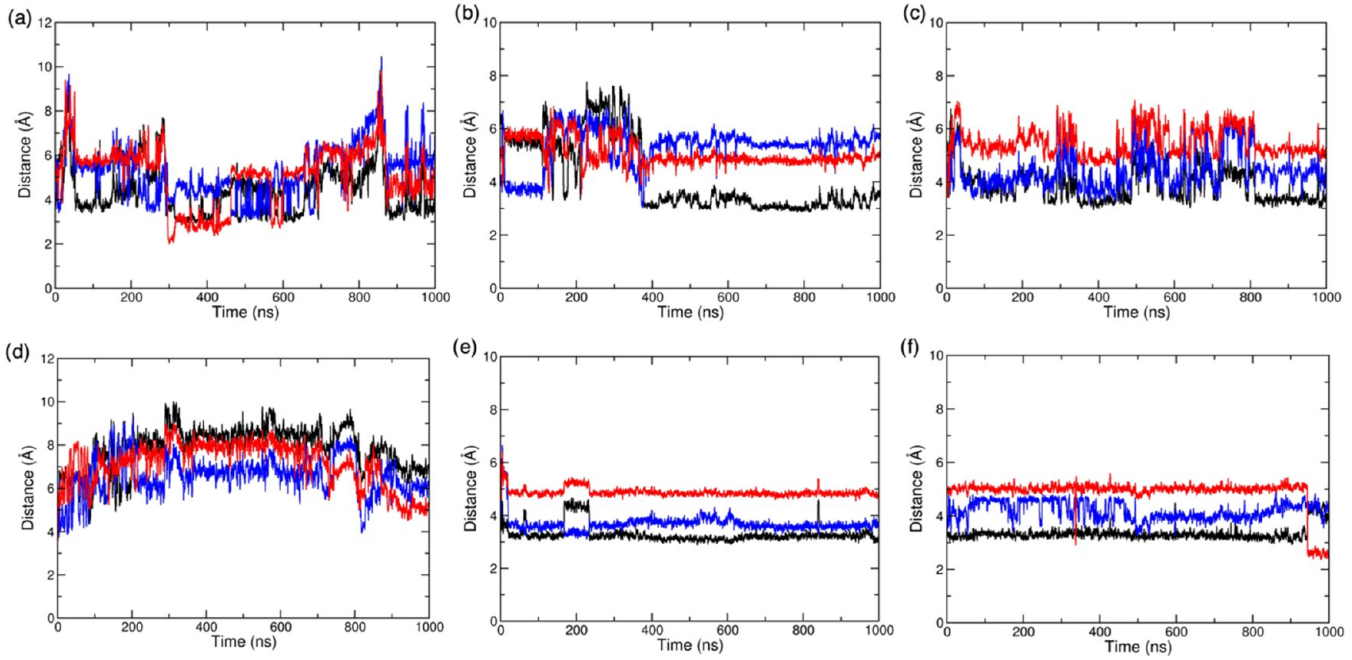

Figure 4. Distance between the ferryl oxygen and first methyl carbon (C1) of the $H3_{1-14}$K9me2 substrate (black), the second methyl carbon (C2) (blue), and hydrogen of the K9 substrate N^{ϵ}-amino group (red) during dynamics at the ferryl intermediate stage of catalysis by the PHF8 SCS variants: (a) I191A, (b) F250A, and (c) N333A and LR variants (d) P221A, (e) H49A, and (f) T74A.

Identification of the Catalytically Relevant SCS and LR Residues

Previous studies with WT PHF8 have revealed key SCS residues involved in substrate binding and catalysis.[45] In particular, binding of the two N^{ϵ}-methyl groups of the $H3_{1-14}$K9me2 substrate is stabilized by interactions with I191 (Figure 2),[45] F250 helps to orientate the N^{ϵ}-methylated lysine side chain of the $H3_{1-14}$K9me2 substrate productively with respect to the ferryl-species, and N333 forms a hydrogen bond with the noncoordinating oxygen of the Fe-coordinating residue D247.[45] Based on these findings, we made in silico substitutions of the key SCS residues I191A, F250A, and N333A. We then performed MD simulations at the ferryl intermediate stage of catalysis, monitoring the effects of the substitutions on the HAT step (Figures S6–S8), followed by QM/MM reaction mechanism studies, with analysis of the frontier molecular orbitals (MOs), EDA, and the intrinsic electric field along the reaction coordinate. The correlated motions between the distant regions of the enzyme and the active site can influence enzyme catalysis and provide a potential mechanistic channel for allosteric regulation.[60,61] We utilized DCCA to identify LR residues in different regions of PHF8 (JmjC regions, the PHD (plant homeobox domain), and the linker region), which are remote to the Fe(IV)-center, but which participate in correlated motions with the Fe(IV)-center and the RC-stabilizing residues in the SCS—I191, F250, and N333. We selected one LR residue from each domain of PHF8, that had a dynamics cross-correlation coefficient larger than 0.20/−0.20 for positive/negative correlated motions with most of the Fe-center and SCS residues. The first such LR residue, P221, is located in the JmjC domain between α6 and β^1, the second, H49, is situated in the PHD domain, and the third, T74, is located in the linker region (Figure 2). P221 has correlated motions with the three SCS residues—I191 (−0.24), F250 (−0.46), and N333 (−0.21), Fe (−0.21), the ferryl oxo (−0.23), Fe-ligating D249 (−0.46), and the substrate H3K9me2 (−0.55). The second LR residue H49 has correlated motions with the three SCS residues—I191 (−0.22), F250 (−0.39) and N333 (−0.23), Fe (−0.22), the ferryl oxo (−0.23), Fe-ligating residues—D249 (−0.36), H247 (−0.17), H249 (−0.15), succinate (−0.24), and the substrate H3K9me2 (−0.37). The third LR residue T74 has correlated motions with the SCS residues I191 (−0.18) and F250 (−0.12), the Fe-ligating residue D249 (−0.11), and the substrate H3K9me2 (−0.22).

To investigate the roles of these residues, we individually changed them to alanine residues. We performed dynamics for each such variant (Figures S9–S11), followed by QM/MM calculations and analysis as for the SCS residues. To comprehensively investigate the effects of the SCS and LR variants on enzyme catalysis, their effects on all reaction steps and/or co-substrate/substrate binding and co-product/product release events should be explored. However, in this manuscript, we focused on a single step −HAT,[45] the rate-limiting step in chemical steps catalyzed by WT PHF8, aiming to explore comprehensively the pathways by which substitutions might influence HAT, including altering correlated motions, RC/TS geometries, orbitals, the intrinsic electric field, and energetic stabilization from other residues.

How Do SCS and LR Residues Influence the HAT RC's Structure and Dynamics?

Binding Orientation of the $H3_{1-14}$K9me2 Substrate. We explored how individually substituting the WT residues in the SCS and LR with alanine residue affects the H3K9me2 substrate orientation with respect to the Fe(IV)-center (Figure 3).

SCS Variants. With the SCS variants, the average distance between the closest methyl (C1) of the H3K9me3 substrate and the ferryl oxygen in the I191A variant (Figure 4) is similar to the analogous WT PHF8 average distance of 4.4 Å (Figure S12). By contrast to WT PHF8, which exhibits a stereo-

https://doi.org/10.1021/jacsau.2c00345
JACS Au 2022, 2, 2169–2186

chemical preference for HAT from the "second" prochiral N^{ϵ}-methyl (C2 in Figure S1),[45] the I191A variant shows a preference for HAT from the first methyl carbon atom (C1 in Figure S1). The I191A substitution creates room in the active site for rotation between the two prochiral methyl carbons and the K9-derived $N^{\epsilon}H$ group of the H3K9me3 substrate. With the F250A and N333A variants, the average distances between the closest methyl (C1) of the $H3_{1-14}K9me2$ substrate and the ferryl oxygen are reduced to 4.1 and 3.8 Å, respectively (Figure 4). For the I191A variant, there is a preference for HAT from the C1 methyl of H3K9me3; with both the F250A and N333A variants instead C2 is preferred, as with WT PHF8.

The results with the three variants indicate that SCS variations in PHF8 can affect the distances between the $H3_{1-14}K9me2$ substrate methyl group and the ferryl oxygen and thus can affect the stereoselectivity of the HAT reaction.

LR Variants. With the P221A LR variant, the distance between the closest methyl (C2) of $H3_{1-14}K9me2$ and the ferryl oxygen increases to an average of 6.5 Å, indicating that the P221A substitution destabilizes productive substrate binding to the Fe(IV)-center (Figure 4). However, in the other two studied LR variants, i.e., H49A and T74A, the first methyl group (C1) of $H3_{1-14}K9me2$ is closest to the ferryl oxygen with shorter distances of 3.2 and 3.3 Å, respectively. The reduced fluctuations between the C1 methyl carbon and the ferryl oxygen with the H49A- and T74A-substituted enzymes further indicate the increased and rigid interactions involving the substrate and Fe(IV)-center in these variants compared to WT PHF8.[45] The average distance between the preferred methyl group of $H3_{1-14}K9me2$ and the ferryl oxygen varied from 3.2 to 6.5 Å in the LR variants compared to a range of 3.8−4.4 Å for the SCS variants and 4.4 Å for WT PHF8. Although distances between the closest methyl group and the ferryl oxygen in some cases might be similar (e.g., varying between 3.3 and 6.5 Å in comparison to 4.4 Å in WT), there is an apparent change in the orientation of the di-methylated amino group of H3K9me2 (Figure 3).

Thus, the LR results indicate that similarly to the SCS variants, the LR variants have the potential to alter the distance between the $H3_{1-14}K9me2$ substrate and the ferryl oxygen, although the magnitude of change is more diverse in the studied LR variant set than the SCS variants.

Hydrogen Bonding Interactions in the SCS and LR Variants. *SCS Variants.* We performed a hydrogen bonding analysis to explore the origin of the distance variations between the substrate $H3_{1-14}K9me2$ and the Fe(IV)-center in the variants at the ferryl stage (Table S1 and Figure S13). In WT PHF8, the $H3_{1-14}K9me2$ substrate is positioned to form a hydrogen bond with F250, and the histone H3R8 in 72 and 70% of the structures from the MD trajectory.[45] In the three SCS variants, the $H3_{1-14}K9me2$ hydrogen bonding interactions with F250 and the histone H3R8 are (i) reduced to 12 and 12% of the MD structures, respectively, in I191A, (ii) reduced to 53% for interactions with F250, and increased to 91% for interactions with H3R8 in the F250A variant, and (iii) increased for both hydrogen bonding interactions to 88 and 83% in the N333A variant.

The local hydrogen bonding/electrostatic interactions in the Fe(IV)-center are altered differently for each SCS variant. With WT PHF8, the non-ferryl-coordinating C4 carboxylate of succinate is positioned to interact with Y257 (83%), N189 (61%), K264 (60%), and T244 (41%).[45] The interactions of the C4 carboxylate of succinate are reduced or absent (with Y257 to 60%, with N189 to 8%, with K264 to 48%, and with T244 to 13%) in the case of the I191A variant. The interactions of the succinate C4 carboxylate in the F250A variant are also reduced, i.e., with Y257 (55%) and N189 (26%), but increased with T244 (to 82%). However, the N333A variant manifested increased interactions of its C4 carboxylate with K264 (72%) and T244 (68%), but a reduced interaction with N189 (51%).

With the SCS variants, the Fe-coordinating D249 is positioned to make hydrogen bonds with the identical residues as in WT PHF8—T253 (75%) and G252 (12%),[45] although there are some variations with the SCS variants. T253 interacts with D249 in 75, 28, and 62% of the I191A, F250A, and N333A MD structures, while G252 is positioned to make hydrogen bonds with D249 in 9, 71, and 14% of the MD structures in I191A, F250A, and N333A, respectively. Similarly to WT PHF8, the two Fe-coordinating histidine residues maintain hydrogen bonding interactions with each other in the I191A (88%) and F250A (84%) variants, but this interaction is somewhat reduced in the N333A variant (61%).

The differences in the stabilizing interactions with the substrate $H3_{1-14}K9me2$ and the Fe(IV)-center in the SCS variants correlate with the K9me2 side-chain orientation and flexibility of the Fe(IV)-center as reflected in the distances of the methylated amino group of $H3_{1-14}K9me2$ to the ferryl oxygen atom, which shows more significant fluctuations in SCS variant dynamics (Figure 4) compared to WT PHF8.[45]

LR Variants. For the LR variants (P221A, H49A, and T74A), hydrogen bonding interactions of the $H3_{1-14}K9me2$ substrate with the protein residues are reduced compared to WT PHF8. For example, the hydrogen bond with F250 (present in 72% of WT MD simulations) is absent in the P221A variant. Instead, the H3K9me3 substrate makes a hydrogen bond with H3R8 (29%). By contrast, with the H49A and T74A variants, the hydrogen bond between the $H3_{1-14}K9me2$ substrate and F250 is present for 84 and 82% of the MD, respectively. The hydrogen bond of the $H3_{1-14}K9me2$ substrate with H3R8 is reduced to 14% of the MD in H49A and is absent for the T74A variant. Overall, these results indicate that the $H3_{1-14}K9me2$ substrate makes fewer hydrogen-bonding interactions in P221A but has increased hydrogen bonding with the H49A and T74A variants compared to WT PHF8. The succinate C4 carboxylate in the P221A variant shows evidence for reduced interactions with Y257 (60%), K264 (56%), and slightly increased interactions with N189 (41%) and T244 (46%) compared to WT PHF8 (Y257 83%, N189 61%, K264 60%, and T244 41%). The C4 carboxylate of succinate in the H49A and T74A variants shows increased interactions with Y257 (87, 85%), K264 (90, 63%), and T244 (90, 56%) but reduced interactions with N189 (35, 40%). The backbone oxygen of the Fe-coordinated D249 residue show hydrogen bonding interactions with T253 (33, 92, 6%) and G252 (26, 7%, not present) in the P221A, H49A, and T74A variants, respectively. The side chain of D249 participates in a hydrogen bonding interaction with N333 (46, 68, 55%) in all three variants, respectively. Further, the two other Fe-coordinating histidines, H247 and H319, participate in hydrogen bonding interactions as observed with WT PHF8.[45]

The reduced interactions between the $H3_{1-14}K9me2$ and Fe(IV)-center in the P221A variant apparently weaken substrate stabilization in the active site and increases the distance between the ferryl oxygen and the $H3_{1-14}K9me2$.

https://doi.org/10.1021/jacsau.2c00345
JACS Au 2022, 2, 2169−2186

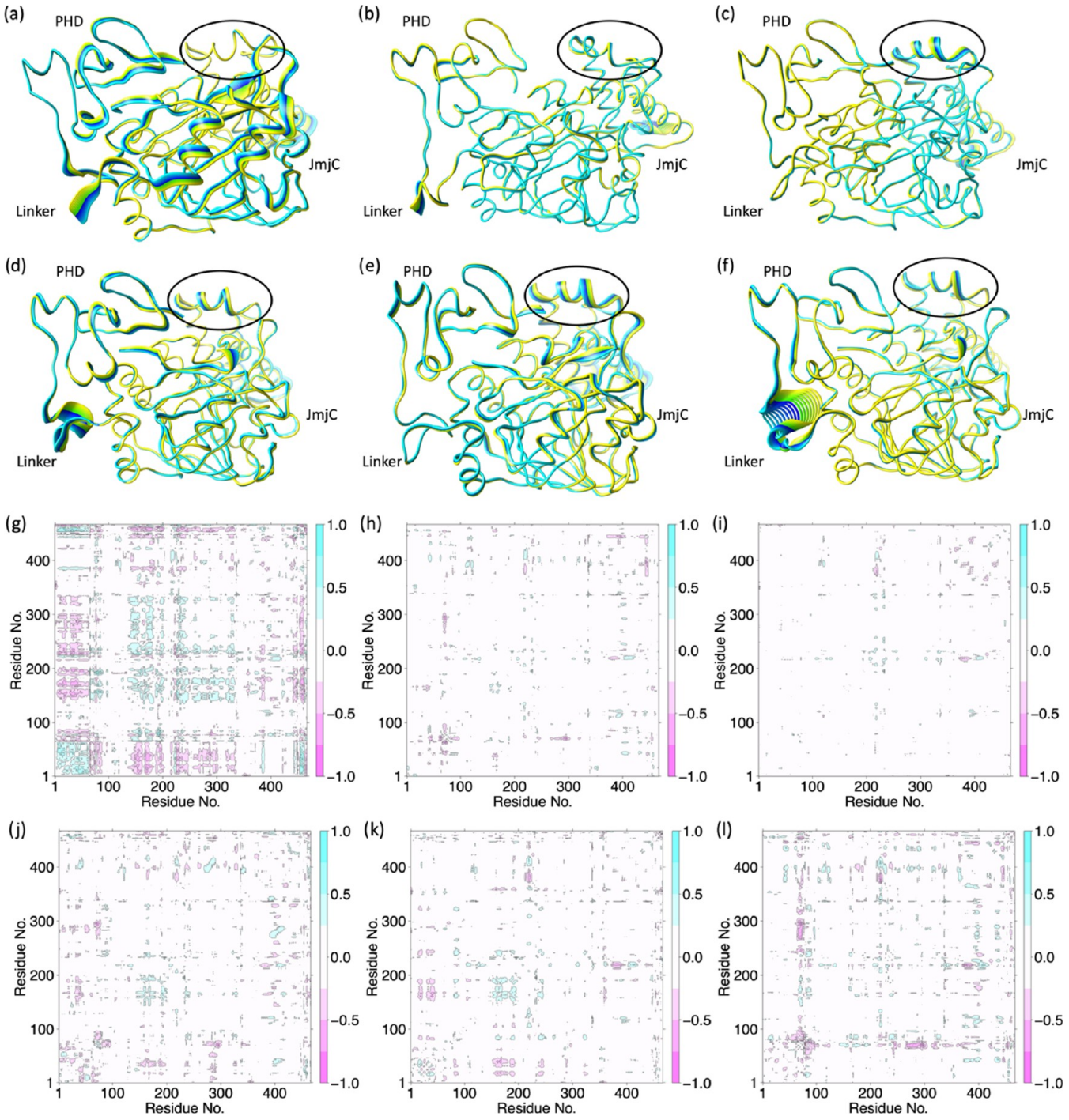

Figure 5. Principle component analysis showing the direction of motions of the most flexible regions of PHF8 SCS variants: (a) I191A, (b) F250A, and (c) N333A, and LR variants: (d) P221A, (e) H49A, and (f) T74A in ferryl intermediate dynamics. The color gradient from yellow to blue indicates the direction of motion. The WT ferryl specific motion of α9 to α12 of JmjC is highlighted with a black oval. Difference DCCA showing correlated motions in the ferryl dynamics of PHF8 SCS variants: (g) I191A, (h) F250A, and (i) N333A, and LR variants: (j) P221A, (k) H49A, and (l) T74A compared to WT PHF8. A positive correlation value (cyan) indicates that the two protein parts move in the same direction. A negative value of correlation (pink) indicates that the direction of motion is in opposite directions.

However, with the H49A and T74A variants, the opposite effects are observed, i.e., the substrate is bound with less conformational flexibility leading to rigid distances between the ferryl oxygen and the $H3_{1-14}$K9me2. These results highlight the potential of LR substitutions to alter the hydrogen bonding interactions in regions distant from the site of variation.

How Do the SCS and LR Residues Influence the Collective Dynamics and Substrate Binding in the HAT RC? *SCS Variants.*

The overall pattern of conformational flexibility and correlated motions of the ferryl intermediate is altered upon substituting the investigated SCS residues. Principal component analysis (PCA) of the WT PHF8 reveals that α9 to α12 (residues 340−440) of the JmjC domain move toward the Fe(IV)-center (Figure S14), leading to tighter binding of the $H3_{1-14}$ substrate.[45] This important motion is lost in both the I191A and F250A variants (Figure 5). For the

https://doi.org/10.1021/jacsau.2c00345
JACS Au 2022, 2, 2169−2186

N333A variant, α9 to α12 are still flexible, but the direction of their motion is not toward the Fe(IV)-center (in contrast to the WT PHF8) (Figure 5). In agreement with these PCA results, free energy calculations using MMGBSA show that the SCS substitutions reduce the binding energy to −93.5 ± 17.9, −92.7 ± 13.9, and −110.7 ± 14.9 kcal/mol in the I191A, F250A, and N333A variants, respectively, compared to the binding energy of −139.0 ± 14.1 kcal/mol in WT PHF8.[45] PCA of I191A also indicates increased motions in several regions of both the enzyme and the $H3_{1-14}$ substrate. In particular, the PHD domain, the linker region, and the α3, α4, and α5 areas of the JmjC domain move toward each other. In contrast to WT PHF8, PCA of the F250A variant shows increased motions in the linker and the C-terminal regions.

Thus, the PCA results indicate that at the ferryl intermediate stage, specific motions of WT PHF8, e.g., the movement of α9 to α12 of the JmjC domain toward the Fe(IV)-center, which leads to tighter binding of the $H3_{1-14}$K9me2 substrate for catalysis, can be either completely lost or altered in SCS variants. The MMGBSA free energy calculations quantify the impact of these motions on substrate binding affinity.

LR Variants. Similarly to SCS variants, the PCA shows that the motion of the α9 to α12 loops toward the Fe(IV)-center for tighter binding of the $H3_{1-14}$K9me2 substrate is lost in the P221A and H49A variations and is highly reduced in the T74A variant (Figure 5). Additionally, PCA of the P221A variant shows that the N-terminal part of the PHD domain and the loop connecting the α11 and α12 loops of the JmjC domain move toward each other. By contrast to the WT, the linker region shows increased motion in the direction away from the JmjC domain. In the H49A variant, PCA analysis indicates that the N-terminal part of the PHD domain moves in the direction of the substrate. The loop connecting the α6 and β^1 regions moves in the direction of the loop connecting α9 to α10 and the loop connecting α11 and α12 of the JmjC domain. PCA analysis indicates that with the T74A variant, the linker region is highly flexible and moves in a direction away from the JmjC domain. The loop connecting α11 and α12 helices move away from the JmjC domain.

The overall PCA results indicate that the movement of α9 to α12 of the JmjC domain toward the Fe(IV)-center, which leads to tighter binding of the $H3_{1-14}$K9me2 substrate for catalysis, is altered by substitutions in PHF8, even when the variations are remote from the Fe(IV)-center. The MMGBSA calculations show that the LR variations reduce the binding energy of the $H3_{1-14}$K9me2 substrate to −98.0 ± 10.5, −114.0 ± 13.9, and −104.0 ± 9.9 kcal/mol for the P221A, H49A, and T74A variants, respectively, compared to a binding energy range of −92.7 to 110.7 kcal/mol for the SCS variants and −139.0 ± 14.1 kcal/mol for the WT.[45] Thus, LR variants can affect the binding of the $H3_{1-14}$K9me2 substrate; however, the binding destabilization is slightly less pronounced compared to the studied SCS variants.

How Do the SCS and LR Residues Influence the Long-Range Correlated Motions in the HAT RC? *SCS Variants.* The SCS residues substantially affect the network of correlated motions of the ferryl complex, as apparent in the differential DCCA plots of the SCS variants compared to WT PHF8 (Figure 5). The differential DCCA plots show the correlated motions that are changed in SCS variants compared to the WT PHF8 ferryl DCCA (Figure S15) by: (i) increases or decreases in the correlation intensities or (ii) changes from correlated to anticorrelated motions or vice versa. The I191A variation increases positively correlated motions within the PHD domain and with part of the $H3_{1-14}$K9me2 substrate. The PHD domain also shows increased negatively correlated motions with the linker, JmjC, and a part of the $H3_{1-14}$K9me2 substrate interacting with the JmjC domain. A region of the JmjC domain (residues 144−201), including α3, β_I^{III}, β_I^{IV}, β_I^{V}, α4, and α5 of the JmjC domain, shows an enhanced positive correlation with the distorted double-stranded β-helix core fold. However, the same region (144−201) indicates negatively correlated motion with the PHD domain, α10 of the JmjC domain, and part of the $H3_{1-14}$K9me2 substrate. The F250A variant induces significant differences in the correlated motions of the linker and α12 of the JmjC domain. The linker region shows an enhanced negative correlation between its residues and parts of the JmjC domain (α1, β^4, α4, α8). α12 of the JmjC domain show negatively correlated motion with the α11 regions of JmjC. The N333A substitution induces an enhanced positive correlated motion of the loop connecting the α1 and β1 with itself and a negative correlation with residues in α10 and α11 of the JmjC domain.

The differential DCCA analyses with the variants highlight communications involving the JmjC and PHD domains, the linker, and $H3_{1-14}$K9me2 substrate are altered upon the SCS variations. Overall, the results indicate that other than local changes, SCS variations have the potential to affect the long-range interactions in the RC for HAT.

LR Variants. The differential DCCA of the P221A variant with respect to WT PHF8 indicates that the P221A substitution increases correlated motions of α10, α11, and α12 of the JmjC domain with other parts of the JmjC and PHD domains (Figure 5). The PHD of the P221A variant also has more anticorrelated motions within itself and regions of the JmjC domain; its linker has increased negatively correlated motions with PHD and JmjC domain. The differential DCCA analyses indicate that the H49A substitution affects the correlated motions of the PHD domain with the linker and JmjC domain. With H49A, the PHD domain has increased anticorrelated motion with the linker and JmjC domain. The region between α4 and β^V of the JmjC domain shows an increased positive correlation with itself and strong anticorrelated motions with the PHD domain. With the H49A variant, α11 and the loop connecting it to α12 show increased correlated motions with the loop connecting the α6 to β^1. The differential DCCA analyses show that the T74A substitution leads to increased anticorrelated motions of the linker region with the JmjC domain and positively correlated motion with the PHD domain. With T74A, the loop connecting α10 to α11 and α11 shows increased anticorrelated motion with α12 of JmjC.

The differential DCCA results reveal that substituting an LR interacting residue in the JmjC, PHD, and linker regions can affect the network of correlated motions involving the catalytic center and other domains. Note that perturbations induced by the LR residues can be more sensitive than those by some SCS residues (e.g., F250A and N333A).

How Do the SCS and LR Variants Influence the HAT Reaction Mechanism?

The HAT step can be rate-limiting in 2OG oxygenase catalysis, including in demethylation by the JmjC demethylases.[19,28,45,62] Therefore, investigating how SCS residues involved in stabilizing and orienting the substrate $H3_{1-14}$K9me2 in the

https://doi.org/10.1021/jacsau.2c00345
JACS Au 2022, 2, 2169−2186

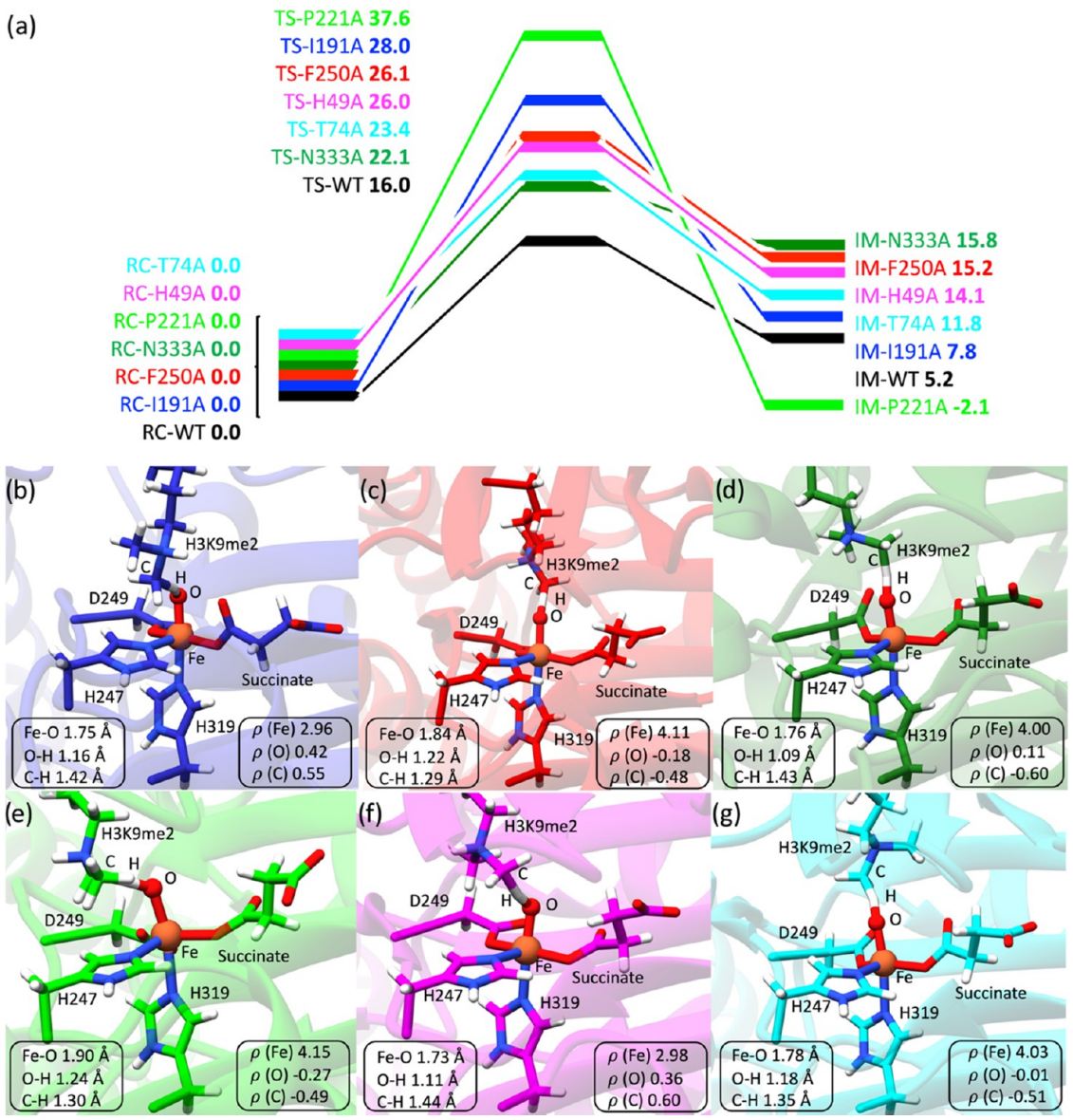

Figure 6. (a) Potential energy surface for HAT mechanism in the SCS and LR PHF8 variants. QM/MM-optimized geometries of HAT transition state of SCS variants: (b) **TS-I191A**, (c) **TS-F250A**, and (d) **TS-N333A**, and LR variants: (e) **TS-P221A**, (f) **TS-H49A**, and (g) **TS-T74A** with key bond lengths (bottom left) and spin densities (bottom right).

WT TS[45] influence HAT is important. Snapshots from well-equilibrated MD trajectories (>500 ns) representing an average MD distance between the ferryl oxygen atom and the methyl carbon (O−C1), and an average angle between the iron, the ferryl oxygen, and the substrate carbon (∠Fe−O−C1), were used to select initial structures for the QM/MM calculations (Table S2).

SCS Variants. The QM/MM-optimized structures of the HAT RCs (Figures S16−S18) for the three SCS variants—**RC-I191A**, **RC-F250A**, and **RC-N333A** show very similar Fe−O bond lengths of 1.61−1.62 Å, spin densities (ranging from 3.09 to 3.16 and from 0.59 to 0.66 on the Fe and oxygen, respectively, Table S3), and charges (Table S4) in agreement with previous QM/MM studies on PHF8[45] and related non-heme Fe enzymes.[28,29,63] The potential energy surfaces (PES) starting from **RC-I191A**, **RC-F250A**, and **RC-N333A** RCs are shown in Figure 6. The energy barriers required to cross the transition states **TS-I191A**, **TS-F250A**, and **TS-N333A** are 28.0, 26.1, and 22.1 kcal/mol, respectively, in comparison to 16.0 kcal/mol for WT PHF8.[45] The [QM(B2 + ZPE)/MM] energies without D3 correction show some minor differences in the HAT activation energies (Table S5), but the overall trend that the selected SCS variants affect the energetics of HAT remains the same. Interestingly, the TS structures differ from WT PHF8 and between the three SCS variants. In particular, the O−H bond is 1.16, 1.22, and 1.09 Å, and the H−C bond is 1.42, 1.29, and 1.43 Å in TS structures **TS-I191A**, **TS-F250A**, and **TS-N333A**, respectively (Figure 6), compared to 1.17 Å (O−H) and 1.34 Å (H−C) in the WT TS structure (Figure S19). Spin density analysis of the TS structures indicates that **TS-F250A** and **TS-N333A** have similar spin densities of 4.11 (**TS-F250A**) and 4.00 (**TS-N333A**) on Fe(IV), compared to 4.06 in WT. The spin densities on the ferryl oxygen are −0.18 in **TS-F250A** and 0.11 in **TS-N333A**, compared to −0.06 in WT. The substrate carbon has a spin density of −0.48 (**TS-F250A**) and −0.60

https://doi.org/10.1021/jacsau.2c00345
JACS Au 2022, 2, 2169−2186

(**TS-N333A**), compared to −0.51 in the WT. However, with **TS-I191A**, the Fe and the ferryl oxygen have a spin density of 2.96 and 0.42, respectively, and the substrate carbon atom has a similar spin density of 0.55. Therefore, the spin density results indicate that similarly to WT PHF8, with **TS-F250A** and **TS-N333A**, an α electron is transferred from the substrate methyl C−H bond to the Fe(IV). By contrast, with **TS-I191A**, the transfer of a β electron from the substrate C−H bond to Fe(IV) occurs.

The HAT reaction results in the formation of a Fe(III)−OH intermediate (**IM**); this reaction is endothermic by 7.8, 15.2, and 15.8 kcal/mol for **IM-I191A**, **IM-F250A**, and **IM-N333A**, respectively (Figures S20−S22), compared to 5.2 kcal/mol for WT PHF8. In the **IM-I191A** intermediate, the Fe−O bond is elongated to 1.79 Å compared to 1.89 Å in the WT. The Fe has a spin density of 2.86 in **IM-I91A** compared to 4.22 in the WT, and the substrate carbon (C1) atom has a spin density of 1.07 compared to −0.96 in the WT. In **IM-F250A** and **IM-N333A** intermediates, the Fe−O bond changes relative to the WT (1.89 Å) to 1.93 and 1.86 Å, respectively. The Fe has spin densities of 4.28 and 4.19, and the spin densities on the substrate carbon (C1) atom are −1.04 and −1.01 for **IM-F250A** and **IM-N333A**, respectively. **IM-F250A** and **IM-N333A** are higher in energy than **IM-I191A**, as the hydroxyl (OH) group in **IM-I191A** is stabilized by a hydrogen bonding interaction with the noncoordinating oxygen atom of succinate; however, such stabilization is absent in the **IM-F250A** and **IM-N333A** structures. For reference, in the WT Fe(III)−OH intermediate (**IM-WT**), the Fe-bound hydroxyl (OH) is stabilized by a hydrogen bond with a nearby water molecule.

The results of these calculations imply that the SCS variations can sensitively alter the rate, the energetics, and the electron transfer pathway of HAT.

LR Variants. Similarly to the **RC-WT** and **RC**s of SCS variants, the QM/MM-optimized ferryl structures (Figures S23−S25) of **RC-P221A**, **RC-H49A**, and **RC-T74A** show Fe−O bond lengths of 1.63, 1.61, 1.61 Å, with corresponding spin densities of 3.20, 3.12, 3.11 and 0.55, 0.65, 0.64 on the Fe and oxygen, respectively (Table S6) and charges (Table S7) in the three LR variants. The energy barriers required to cross the TS in **TS-P221A**, **TS-H49A**, **and TS-T74A** are 35.7, 26.0, and 23.4 kcal/mol compared to 16.0 kcal/mol for WT PHF8. In comparison, the SCS variants show an energy barrier ranging between 22.1 and 28.0 kcal/mol (Figure 6). The [QM(B2 + ZPE)/MM] energies without D3 correction also indicate that the selected LR variants affect the energetics of HAT (Table S5). The energy barrier for the P221A LR variant is the highest, although P221 is located relatively far away from the active site. The reason for this is that the P221A substitution profoundly affects substrate binding. The average distance between the closest methyl group of H3K9me2 substrate to the ferryl oxygen increases to 6.5 Å in the P221A variant compared to 4.4 Å in WT. To further investigate this observation, we selected two structures from the QM/MM PES with a shorter distance between the H3K9me2 substrate and ferryl oxygen atom, namely, 4.5 and 3.5 Å. However, after free QM/MM optimization, both structures relaxed to a structure with similar large distances of 6.1 and 6.2 Å, respectively. The increased distance correlates with an increased HAT barrier, as demonstrated in studies with a related 2OG-dependent enzyme, KDM4A.[28] The results also agree with another similar 2OG-dependent enzyme TET2, where several clinical variants far away from the active site were found to play an important role in TS stabilization and significantly affect HAT barriers, the distance of the substrate methyl from the ferryl oxygen, and the electron transfer mechanism.[22,29,64]

The TS structures of **TS-P221A**, **TS-H49A**, and **TS-T74A** have O−H bond lengths of 1.24, 1.11, and 1.18 Å, and H−C1 bond lengths of 1.30, 1.44, and 1.35 Å in, respectively, compared to an O−H bond length of 1.09−1.22 Å, and H−C1 bond length of 1.29−1.43 Å in the SCS variants (Figure 6). The spin density analysis of the TS structures indicates that **TS-P221A** and **TS-T74A** have similar spin densities of 4.15 and 4.03 on Fe with a spin density of −0.27 and −0.01 on the ferryl oxygen atom, similar to the spin densities in **TS-WT**, and the SCS variant **TS-F250A**, **TS-N333A**. However, as in the case of SCS variant **TS-I191A**, spin density analysis of the **TS-H49A** indicates that the Fe and the ferryl oxygen have spin densities of 2.98 and 0.36, respectively. Similarly, the substrate carbon atom has similar spin densities of −0.49 and −0.51 in the **TS-P221A** and **TS-T74A** structures but a positive spin density of 0.60 in the case of the **TS-H49A** structure (Table S6). Therefore, the spin density results indicate that similarly to the WT PHF8 and the SCS variants (**TS-F250A** and **TS-N333A**), an α electron is transferred from the substrate C−H bond to the ferryl in **TS-P221A** and **TS-T74A**. By contrast, with **TS-H49A** transfer of a β electron from the substrate C−H bond to the ferryl occurs, as with the SCS variant **TS-I191A**. Similar results were reported in a TET2 double-variant K1299E-S1303N, where variations far away from the Fe(IV)-center changes the electron transfer mechanism in HAT from an α electron (σ channel) to a β electron transfer (π channel).[29]

As the HAT is completed, an Fe(III)−OH (**IM-P221A**, **IM-H49A**, and **T74A**) intermediate is generated (Figures S26−S28); the HAT reaction is exothermic for P221A by −2.1 kcal/mol but endothermic by 14.1, and 11.8 kcal/mol for H49A and T74A, respectively, compared to values of 5.2 kcal/mol for WT and 7.8−15.8 in the SCS variants. The Fe has a spin density of 4.23, 2.88, and 4.21 with a spin density of −1.08, 1.07, and −1.07 on the substrate N^{ϵ}-linked carbon (C1) atom in the three **IM-P221A**, **IM-H49A**, and **IM-T74A** intermediate. The reaction energy is lower in the case of P221A because, similarly to WT and the I191A SCS variant, in the **IM-P221A**, the Fe(III)−OH hydroxyl is stabilized by a hydrogen bond with two water molecules; however, such stabilization of hydroxyl is missing in the **IM-H49A** and **IM-T74A** structures. Thus, the HAT calculations on the LR variants indicate that variations in the remote regions of an enzyme having correlated motions with the active site can substantially alter the energy barrier for HAT, i.e., to 35.7, 26.0, and 23.4 kcal/mol in the P221A, H49A, and T74A variants compared to 16.0 kcal/mol for the WT and a range of 22.1−28.0 kcal/mol for the SCS variants. Overall, the results indicate that LR variants can have a broad-ranging effect on the energetics of HAT and, as for the SCS variants, can alter the electron transfer pathway of HAT.

Factors Affecting the HAT in SCS and LR Variants

Individual Energetic Residue Contributions to the TS Stabilization. Variations in residues that energetically stabilize the TS can be a powerful tool to modulate the rate of enzyme reactions.[65,66] We applied EDA[58,59] to extract the individual energetic contributions of residues involved in the TS stabilization in the SCS variants (Figure 7).

https://doi.org/10.1021/jacsau.2c00345
JACS Au 2022, 2, 2169−2186

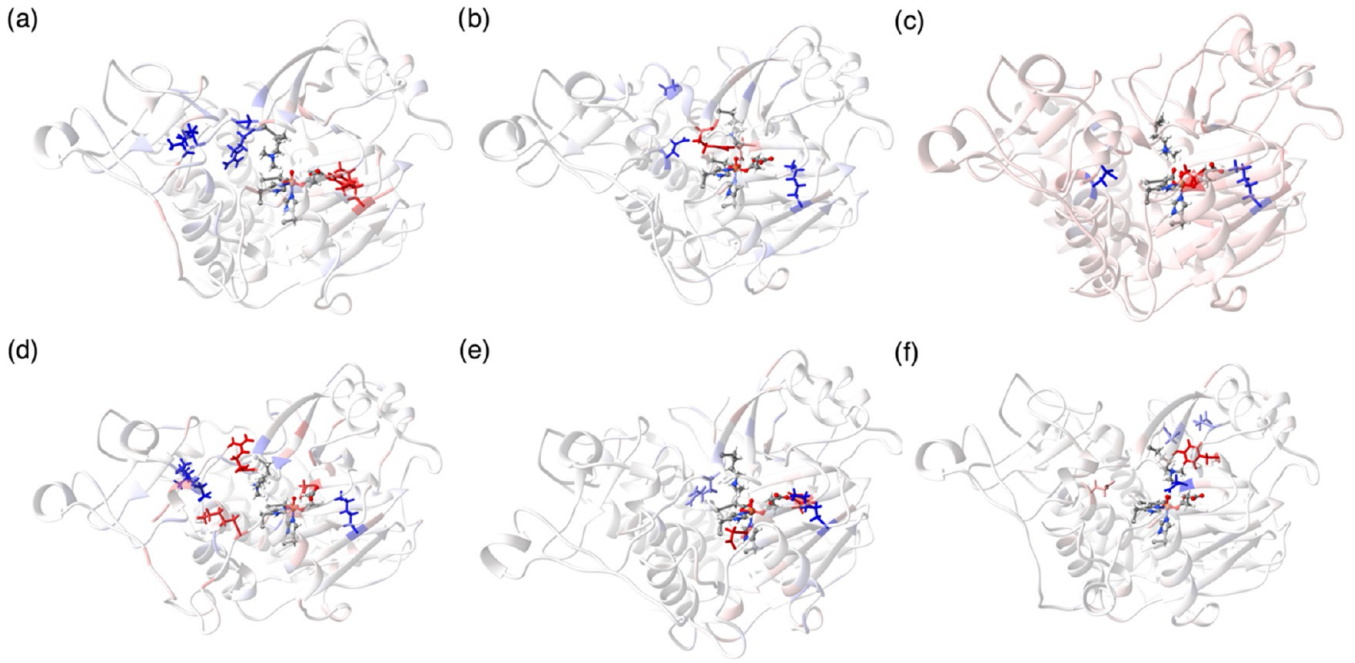

Figure 7. Primary residues stabilizing (blue) and destabilizing (red) for the HAT TS around the Fe(IV)-center in SCS variants: (a) I191A, (b) F250A, and (c) N333A, and LR variants: (d) P221A, (e) H49A, and (f) T74A.

SCS Variants. In the case of the **TS-I191A**, in addition to the H3R8 stabilization by −2.2 kcal/mol, other residues of the histone substrate—H3K4me3 and H3A7—contribute to TS stabilization, i.e., by −2.8 and −2.5 kcal/mol. The primary residues that destabilize the **TS-I191A**, Y257, and K264 (by 2.0 and 1.7 kcal/mol, respectively) are different from the L169 and T244, which are the primary destabilizing residues in WT PHF8. EDA of **TS-F250A** indicates that H3R8, which had a TS stabilizing effect in WT PHF8, and N333 are primary destabilizing residues (by 2.6 and 1.1 kcal/mol, respectively). The primary residues stabilizing the **TS-F250A** are E350 and K264, by −1.3 and −1.1 kcal/mol, respectively. Note that K264 acts as a TS destabilizing residue in the case of **TS-I191A**. EDA analysis of the N333A shows, as for the **TS-F250A**, that E350 and K264 play a TS stabilizing role by −1.4 and −1.2 kcal/mol, respectively. However, the primary destabilizing residues in the case of **TS-F250A** are T244 and I191, which destabilize the **TS-F250A** by 1.0 and 0.5 kcal/mol. The individual energetic contributions of other PHF8 and $H3_{1-14}$K9me2 substrate residues toward TS stabilization in SCS variants are given in the SI (Figures S29−S31).

These results indicate that SCS variations can alter the individual energetic contributions of residues toward TS stabilization and can even entirely change a residue's role from TS stabilizing residue to TS destabilizing. Thus, e.g., K264, which does not contribute to TS stabilization/destabilization in WT PHF8, acts as a TS stabilizing residue in the F250A and N333A variants but a TS destabilizing residue in the I191A variant.

LR Variants. Similarly to the SCS variants, we explored how the individual energetic contributions of the HAT TS stabilizing residues differed using EDA in the three tested LR variants (Figure 7). In the case of the **TS-P221A** intermediate, the histone substrate residue, i.e., H3K4me3, as well as E39 and K264, contribute to TS stabilization by −6.2, −7.7, and −6.6 kcal/mol, respectively. R164, K81, and N333 are primary residues destabilizing the **TS-P221A**, i.e., by 4.5, 3.4, and 3.3 kcal/mol, respectively. Among these residues, H3K4me3, K264, and N333 play either a TS stabilizing or destabilizing role in WT and the SCS variants. E39 in the PHD domain and K81 in the linker region appear to be key residues in TS stabilizing or destabilizing interactions. EDA analysis of **TS-H49A** indicates that H3R8, which plays a role in TS stabilizing residues in WT PHF8, and K264 are important residues that stabilize the TS by −0.3 and −0.8 kcal/mol, respectively; D245 and Y257 are important residues that destabilize the TS, i.e., by 0.8 and 0.6 kcal/mol, respectively. D158 of the JmjC domain plays a TS stabilizing role in LR variant H49A but is not seen as the primary stabilizing/destabilizing residue in the EDA of WT or the SCS variants. EDA analysis of the T74A shows that N333, and D158, the latter of which is a unique residue not seen in WT or SCS variants, play a TS stabilizing role by −4.5 and −1.8 kcal/mol, respectively. However, the primary destabilizing residues for **TS-T74A** are Y234 and E350, which destabilize the TS by 4.4 and 1.4 kcal/mol, respectively. The individual energetic contributions of other PHF8 and $H3_{1-14}$K9me2 substrate residues toward TS stabilization in LR variants are given in the SI (Figures S32−S34).

Thus, the results indicate that LR variations can alter the individual energetic contributions of protein residues that contribute toward TS stabilization/destabilization in WT and SCS variants, along with additional residues away from the Fe(IV)-center. An example is Y234, which contributes to stabilizing the HAT TS in WT PHF8, but acts as a TS destabilizing residue in the T74A variant.

Effect of SCS and LR Variations on the Intrinsic Electric Field along the Reaction Coordinate. Recent advances in research in electric field effects have highlighted how orienting an electric field along a "reaction-axis" can affect the rate of catalysis and even selectivity.[67,68] One study has shown that changes in the electric field can affect the rate of HAT in synthetic metalloenzyme analogs.[43] We used the TITAN program[69] to compare how the intrinsic electric field

https://doi.org/10.1021/jacsau.2c00345
JACS Au 2022, 2, 2169−2186

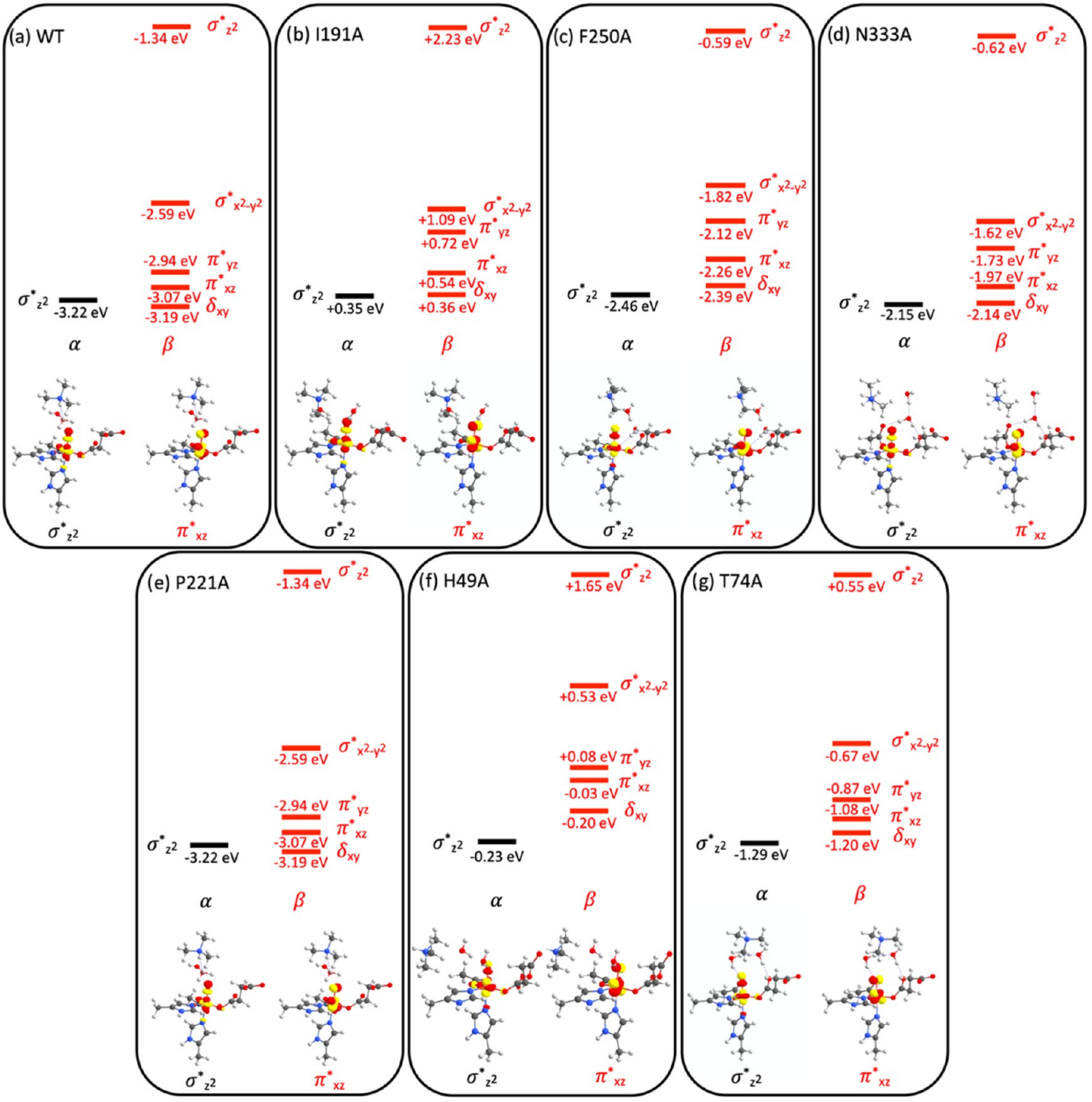

Figure 8. FMOs for HAT mechanism and their energies in RCs of (a) PHF8 WT (for comparison), and SCS PHF8 variants: (b) I191A, (c) F250A, and (d) N333A, and LR variants: (e) P221A, (f) H49A, and (g) T74A.

of the ferryl is affected, along the Fe═O bond direction, as a function of the SCS and LR variations.

SCS Variants. Intrinsic electric field calculations on all of the three **RC-I191A**, **RC-F250A**, and **RC-N333A** show reduced values of −0.0257, −0.0255, and −0.0254 au, respectively, compared to −0.0272 au in **RC-WT**. The reduced electric field along the direction of the Fe═O bond compared to **RC-WT** correlates with the increase in the HAT barrier for the three SCS variants. The results suggest that one role of the SCS residues might be to maintain the required electric field in the active site and that substitution of these residues can affect the intrinsic electric field and thus the HAT.

LR Variants. Intrinsic electric field calculations of all of the three LR variants **RC-P221A**, **RC-H49A**, and **RC-T74A** give values of −0.03268, −0.02779, and −0.02448 au, respectively, compared to an intrinsic electric field of −0.0272 au in WT, and a range of −0.00254 to −0.00257 au observed for the SCS variants. The results indicate that the LR variants can affect the intrinsic electric field of PHF8, and contrary to the SCS variations investigated, remote residues can be substituted to increase, maintain or reduce the intrinsic electric field of the enzyme.

Influence of SCS and LR Variants on the FMOs for HAT. The analysis described in this section elaborates on the possibility that the SCS and LR variants can influence the

https://doi.org/10.1021/jacsau.2c00345
JACS Au 2022, 2, 2169−2186

energy differences between the FMOs involved in HAT. For this purpose, similarly to a previous study on the 2OG oxygenase TauD enzyme,[70] we compared the relative energy difference between the two competing acceptor orbitals for each system.

SCS Variants. We performed MO analysis on the I191A, F250A, and N333A variants to explore how these SCS variations affect the electronic structure properties of the ferryl intermediate, the nature of the acceptor frontier MO orbital, and the electron transfer mechanism in HAT. Similarly to **RC-WT**,[45] all of the three **RC-I191A**, **RC-F250A**, and **RC-N333A** show an electronic occupancy of $\delta_{xy}{}^1\pi^*_{xz}{}^1\pi^*_{yz}{}^1\sigma^*_{x^2-y^2}{}^1\sigma^*_{z^2}{}^0$ at the quintet spin state. The calculations show that the $\sigma^*_{z^2}$ is still the LUMO in the three variants, but the energy splitting between the $\sigma^*_{z^2}$ and the π^*_{xz} orbitals is increased to 0.19 eV (4.38 kcal/mol), 0.20 eV (4.61 kcal/mol), and 0.18 eV (4.15 kcal/mol) in **I191A-RC**, **F250A-RC**, and **N333A-RC**, respectively (Figure 8). TS orbital analysis indicates that, as for WT PHF8, the HAT acceptor orbital is the $\sigma^*_{z^2}$ orbital for the **TS-F250A** and **TS-N333A**. However, for the **TS-I191A** variant, the π^*_{xz} orbital acts as an electron acceptor orbital for hydrogen atom abstraction even though the π^*_{xz} orbital is higher in energy than the $\sigma^*_{z^2}$ orbital in **RC-I191A**.

These results are supported by spin density analysis of the substrate carbon atom. A residual positive spin density (0.55) on the carbon atom of the substrate in **TS-I191A** indicates that a β electron is transferred to the Fe(IV)-center. By contrast, a residual negative spin density of −0.48 and −0.60 in **TS-F250A** and **TS-N333A** means that an α electron is transferred to the Fe(IV)-center. The reason for a π^* electron transfer in **TS-191A** is not the energy difference between the FMOs but is due to the constrained ∠Fe−O−H in the **TS-I191A**, i.e., 117° compared to 133 and 166° in **TS-F250A** and **TS-N333A**, respectively. These results highlight the potential for SCS residue substitutions to increase the energy gap between the FMOs for HAT; however, the steric/orientation factors in the I191A variant constitute a significant factor in the switch from σ- to π-electron transfer channel in HAT.

LR Variants. We analyzed differences between the individual energies of the frontier MOs in the HAT reaction to explore how the LR substitutions affect the electronic structure properties of the ferryl intermediate and the electron transfer pathway. Similarly to the **RC-WT** and the three SCS variants, the RCs of all of the three LR variants, **RC-P221A**, **RC-H49A**, and **RC-T74A**, show an electronic occupancy of $\delta_{xy}{}^1\pi^*_{xz}{}^1\pi^*_{yz}{}^1\sigma^*_{x^2-y^2}{}^1\sigma^*_{z^2}{}^0$ with a quintet spin state. The calculations show that the $\sigma^*_{z^2}$ is the LUMO in the three variants. The energy splitting between the $\sigma^*_{z^2}$ and the π^*_{xz} orbital is increased to 0.203 eV (4.68 kcal/mol), 0.137 eV (3.15 kcal/mol), and 0.218 eV (5.02 kcal/mol) in **RC-P221A**, **RC-H49A**, and **RC-T74A**, respectively, compared to an energy split of 2.76 kcal/mol for WT PHF8 and 4.38−4.61 kcal/mol in the SCS variants (Figure 8). The TS orbital analysis indicates that similar to **TS-WT**,[45] the HAT acceptor orbital for the **TS-P221A** and **TS-T74A** is the $\sigma^*_{z^2}$ orbital. However, for the **TS-H49A** variant, the π^*_{xz} orbital acts as an electron acceptor orbital for hydrogen atom abstraction, even though it is higher in energy than the $\sigma^*_{z^2}$ orbital in the reactant complex **RC-H49A**. As for SCS variant I191A, an important reason for a π^* electron transfer in **TS-H49A** could be the constrained ∠Fe−O−H in the **TS-H49A**, which has a value of 119° compared to values of 124 and 144° in **TS-P221A** and **TS-T74A**, respectively. In an ideal case, a Fe−O−H angle of 180° is preferred for effective σ^* transfer and a Fe−O−H angle of 120° is preferred for π^* transfer.[14] However, numerous cases in the literature are reported for σ^* transfer at angles lower than the ideal of 180°.[63,71,72] For **TS-P221A** (with a Fe−O−H angle of 123.9°), both the spin density analysis and the natural/spin natural orbitals support a mechanism involving electron transfer via the σ^* pathway. Indeed, the non-ideal angle may contribute to an increased energy barrier for HAT, as indicated for the P221A variant. Thus, the calculations show that, similarly to the SCS variants, the LR variants can alter the preferred channel for the electron transfer and increase the energy gap between the two FMOs in HAT.

CONCLUSIONS

Rational modulation of the efficiency and selectivity of HAT in metalloenzymes remains a challenge. The ability of SCS and LR residues to alter activity and mechanisms makes them an excellent target for enzyme engineering, but the motions of these residues during specific steps in catalysis are challenging to study by experimental methods. To efficiently provide guidance on redesigning enzymes for more effective HAT in catalysis, we need to understand how residues in the SCS and LR regions influence different aspects of the HAT reaction. Importantly, there is little systematic knowledge concerning the "redesign potential" of residues in the SCS and LR enzyme regions.

For PHF8, we identified (i) three SCS residues critical for stabilizing a productive orientation of the H3K9me2 substrate, the Fe-ligand D191, and (ii) three LR residues from different domains of PHF8 using DCCA (see the Section 3 for details). To investigate the potential of the identified SCS and LR residues to influence the HAT step in PHF8 catalysis, we performed MD simulations and QM/MM mechanism calculations on selected PHF8 variants. Importantly, the computational methods applied in this study predicted the lack of activity for the clinical variant F279S in agreement with the experimental data[48] and have been previously used to reproduce the effects of multiple mutations in other 2OG-dependent oxygenases, i.e., KDM4A, TET2, and EFE.[28−30] The study identified multiple mechanistic pathways by which SCS and LR residues can influence HAT, including by affecting the activation energy, electron transfer mechanism, structures, and flexibilities of the RC and TS, interdomain correlated motions, and by altering the intrinsic electric field of the enzyme.

PCA of three SCS variants (I191A, F250A, and N333A) reveals that the ferryl intermediate specific motion of α9 to α12 of JmjC toward the Fe(IV)-center, which enables tight binding of the $H3_{1-14}$K9me2 substrate in WT PHF8, is lost or heavily altered in the tested SCS variants. This loss of motion in the SCS variants leads to weaker binding of the $H3_{1-14}$K9me2 substrate than WT PHF8, as supported by MMGBSA calculations. The MD results also demonstrate that the SCS variations alter hydrogen bonding interactions of the $H3_{1-14}$K9me2 substrate and Fe(IV)-center such that the WT preference for HAT from C2 methyl carbon of $H3_{1-14}$K9me2 is not maintained in all three variants indicating that SCS variations can modulate the specificity of HAT mechanism. The QM/MM calculations indicate that SCS variants increase the activation energy of the HAT considerably to 22.1−28.0 kcal/mol compared to 16.0 kcal/mol for WT PHF8. Further analysis of the mechanistic aspects of HAT shows that SCS residues can: (i) either modulate the individual residue energy

https://doi.org/10.1021/jacsau.2c00345
JACS Au 2022, 2, 2169−2186

contribution toward the TS stabilization or can change an individual residue's role from TS stabilizing to a TS destabilizing; (ii) reduce the intrinsic electric field of PHF8 enzyme along the ferryl Fe═O bond direction, thus increasing the activation energy; (iii) alter the molecular orbitals involved in electron transfer during HAT.

PCA of the three LR variants, P221A, H49A, and T74A, shows that the LR variations can affect the specific motions of α9 to α12 of JmjC toward the Fe(IV)-center. However, the MMGBSA calculations show that the $H3_{1-14}$K9me2 substrate binding is less destabilized in the LR variants than in the SCS variants. MD studies of the LR variants show that even though the substitution site is far from the active site, it can still affect the hydrogen bonding interactions of the Fe(IV)-center and the $H3_{1-14}$K9me2 substrate. Compared to the SCS variants, where only the stereochemical preference for the $H3_{1-14}$K9me2 substrate's N^{ε}-methyl group was affected, the LR variants can alter both the stereochemical preference and overall distance of the $H3_{1-14}$K9me2 substrate from the Fe(IV)-center. The results of QM/MM calculations for the HAT process indicate that the LR variants (P221A, H49A, and T74A) require potential energy in the range of 23.4−35.7 kcal/mol compared to 16.0 kcal/mol for the WT and 22.1−28.0 kcal/mol for the SCS variants (I191A, F250A, and N333A). Thus, the results demonstrate that, compared to the SCS variants, the LR variants can exercise a broader ranging effect on the energy requirement of HAT. The EDA results indicate that the LR variations alter the individual energetic contributions of residues that contribute to the stabilization/destabilization of the TS in WT and SCS variant catalysis (along with other residues). The LR variations also alter the magnitude of the intrinsic electric field of the protein to either increase, maintain, or reduce it compared to WT PHF8. Interestingly, MO analyses indicate that similarly to the SCS variations, LR variations can alter the molecular orbital mechanism for HAT.

Overall, the results indicate that, at least for the tested PHF8 variants, both SCS and LR substitutions can be used as tools in enzyme redesign to modulate the specificity and efficiency of the HAT step. The study develops a novel framework for identifying catalytically relevant residues through analysis of correlated motions and conceptualizes the diverse mechanistic pathways of influence of the SCS/LR interactions on HAT in PHF8 and, by implication other 2OG oxygenases.

■ ASSOCIATED CONTENT

Supporting Information

The Supporting Information is available free of charge at https://pubs.acs.org/doi/10.1021/jacsau.2c00345.

Additional analysis of molecular dynamics trajectories and QM/MM-optimized geometries with spin densities and Mulliken charges (PDF)

■ AUTHOR INFORMATION

Corresponding Author

Christo Z. Christov − *Department of Chemistry, Michigan Technological University, Houghton, Michigan 49931, United States;* orcid.org/0000-0002-4481-0246; Email: christov@mtu.edu

Authors

Shobhit S. Chaturvedi − *Department of Chemistry, Michigan Technological University, Houghton, Michigan 49931, United States;* orcid.org/0000-0003-4977-5600

Simahudeen Bathir Jaber Sathik Rifayee − *Department of Chemistry, Michigan Technological University, Houghton, Michigan 49931, United States;* orcid.org/0000-0001-8557-078X

Sodiq O. Waheed − *Department of Chemistry, Michigan Technological University, Houghton, Michigan 49931, United States;* orcid.org/0000-0003-3422-4531

Jon Wildey − *Department of Chemical Engineering, Michigan Technological University, Houghton, Michigan 49931, United States*

Cait Warner − *Department of Biological Sciences, Michigan Technological University, Houghton, Michigan 49931, United States*

Christopher J. Schofield − *The Chemistry Research Laboratory, Department of Chemistry and the Ineos Oxford Institute for Antimicrobial Research, University of Oxford, Oxford OX1 3TA, United Kingdom;* orcid.org/0000-0002-0290-6565

Tatyana G. Karabencheva-Christova − *Department of Chemistry, Michigan Technological University, Houghton, Michigan 49931, United States;* orcid.org/0000-0001-8629-4377

Complete contact information is available at: https://pubs.acs.org/10.1021/jacsau.2c00345

Notes

The authors declare no competing financial interest.

■ ACKNOWLEDGMENTS

This research is supported by the National Institute Of General Medical Sciences of the National Institutes of Health under Award Number R15GM139118 to C.Z.C and C.J.S. C.J.S. thanks Cancer Research UK, and the Biotechnology and Biological Research Council for funding.

■ REFERENCES

(1) Mayer, J. M. Understanding Hydrogen Atom Transfer: From Bond Strengths to Marcus Theory. *Acc. Chem. Res.* **2011**, *44*, 36−46.

(2) de Visser, S. P.; Kumar, D., Eds. *Iron-Containing Enzymes: Versatile Catalysts of Hydroxylation Reactions in Nature*; Royal Society of Chemistry: Cambridge, 2011.

(3) Cheng, L.; Wang, H.; Cai, H.; Zhang, J.; Gong, X.; Han, W. Iron-Catalyzed Arene C−H Hydroxylation. *Science* **2021**, *374*, 77−81.

(4) Shang, R.; Ilies, L.; Nakamura, E. Iron-Catalyzed C−H Bond Activation. *Chem. Rev.* **2017**, *117*, 9086−9139.

(5) Gandeepan, P.; Müller, T.; Zell, D.; Cera, G.; Warratz, S.; Ackermann, L. 3d Transition Metals for C−H Activation. *Chem. Rev.* **2019**, *119*, 2192−2452.

(6) Dalton, T.; Faber, T.; Glorius, F. C−H Activation: Toward Sustainability and Applications. *ACS Cent. Sci.* **2021**, *7*, 245−261.

(7) Warren, J. J.; Tronic, T. A.; Mayer, J. M. Thermochemistry of Proton-Coupled Electron Transfer Reagents and Its Implications. *Chem. Rev.* **2010**, *110*, 6961−7001.

(8) Shaik, S.; Kumar, D.; de Visser, S. P.; Altun, A.; Thiel, W. Theoretical Perspective on the Structure and Mechanism of Cytochrome P450 Enzymes. *Chem. Rev.* **2005**, *105*, 2279−2328.

(9) Mandal, D.; Mallick, D.; Shaik, S. Kinetic Isotope Effect Determination Probes the Spin of the Transition State, Its Stereochemistry, and Its Ligand Sphere in Hydrogen Abstraction

Reactions of Oxoiron(IV) Complexes. *Acc. Chem. Res.* **2018**, *51*, 107−117.
(10) Evans, M. G.; Polanyi, M. Inertia and Driving Force of Chemical Reactions. *Trans. Faraday Soc.* **1938**, *34*, 11.
(11) Sutin, N.Theory of Electron Transfer Reactions: Insights and Hindsights. In *Progress in Inorganic Chemistry*; Lippard, S. J., Ed.; John Wiley & Sons, Inc.: Hoboken, NJ, 2007; pp 441−498.
(12) de Visser, S. P.; Lin, Y.-T.; Ali, H. S.; Bagha, U. K.; Mukherjee, G.; Sastri, C. V. Negative Catalysis / Non-Bell-Evans-Polanyi Reactivity by Metalloenzymes: Examples from Mononuclear Heme and Non-Heme Iron Oxygenases. *Coord. Chem. Rev.* **2021**, *439*, No. 213914.
(13) Solomon, E. I.; Light, K. M.; Liu, L. V.; Srnec, M.; Wong, S. D. Geometric and Electronic Structure Contributions to Function in Non-Heme Iron Enzymes. *Acc. Chem. Res.* **2013**, *46*, 2725−2739.
(14) Shaik, S.; Chen, H.; Janardanan, D. Exchange-Enhanced Reactivity in Bond Activation by Metal−Oxo Enzymes and Synthetic Reagents. *Nat. Chem.* **2011**, *3*, 19−27.
(15) Ye, S.; Neese, F. Quantum Chemical Studies of C−H Activation Reactions by High-Valent Nonheme Iron Centers. *Curr. Opin. Chem. Biol.* **2009**, *13*, 89−98.
(16) Ye, S.; Geng, C.-Y.; Shaik, S.; Neese, F. Electronic Structure Analysis of Multistate Reactivity in Transition Metal Catalyzed Reactions: The Case of C−H Bond Activation by Non-Heme Iron(Iv)−Oxo Cores. *Phys. Chem. Chem. Phys.* **2013**, *15*, 8017.
(17) Wojdyla, Z.; Borowski, T. Properties of the Reactants and Their Interactions within and with the Enzyme Binding Cavity Determine Reaction Selectivities. The Case of Fe(II)/2-Oxoglutarate Dependent Enzymes. *Chem.—Eur. J.* **2022**, *28*, No. e202104106.
(18) Ghafoor, S.; Mansha, A.; de Visser, S. P. Selective Hydrogen Atom Abstraction from Dihydroflavonol by a Nonheme Iron Center Is the Key Step in the Enzymatic Flavonol Synthesis and Avoids Byproducts. *J. Am. Chem. Soc.* **2019**, *141*, 20278−20292.
(19) Schofield, C.; Hausinger, R., Eds. *2-Oxoglutarate-Dependent Oxygenases*, Royal Society of Chemistry: Cambridge, 2015.
(20) Visser, S. P. Second-Coordination Sphere Effects on Selectivity and Specificity of Heme and Nonheme Iron Enzymes. *Chem.—Eur. J.* **2020**, *26*, 5308−5327.
(21) Martinez, S.; Fellner, M.; Herr, C. Q.; Ritchie, A.; Hu, J.; Hausinger, R. P. Structures and Mechanisms of the Non-Heme Fe(II)- and 2-Oxoglutarate-Dependent Ethylene-Forming Enzyme: Substrate Binding Creates a Twist. *J. Am. Chem. Soc.* **2017**, *139*, 11980−11988.
(22) Hu, L.; Li, Z.; Cheng, J.; Rao, Q.; Gong, W.; Liu, M.; Shi, Y. G.; Zhu, J.; Wang, P.; Xu, Y. Crystal Structure of TET2-DNA Complex: Insight into TET-Mediated 5mC Oxidation. *Cell* **2013**, *155*, 1545−1555.
(23) Abidi, F.; Miano, M.; Murray, J.; Schwartz, C. A Novel Mutation in the PHF8 Gene Is Associated with X-Linked Mental Retardation with Cleft Lip/Cleft Palate. *Clin. Genet.* **2007**, *72*, 19−22.
(24) Zoi, I.; Suarez, J.; Antoniou, D.; Cameron, S. A.; Schramm, V. L.; Schwartz, S. D. Modulating Enzyme Catalysis through Mutations Designed to Alter Rapid Protein Dynamics. *J. Am. Chem. Soc.* **2016**, *138*, 3403−3409.
(25) Schafer, J. W.; Zoi, I.; Antoniou, D.; Schwartz, S. D. Optimization of the Turnover in Artificial Enzymes via Directed Evolution Results in the Coupling of Protein Dynamics to Chemistry. *J. Am. Chem. Soc.* **2019**, *141*, 10431−10439.
(26) Rabe, P.; Kamps, J. J. A. G.; Sutherlin, K. D.; Linyard, J. D. S.; Aller, P.; Pham, C. C.; Makita, H.; Clifton, I.; McDonough, M. A.; Leissing, T. M.; Shutin, D.; Lang, P. A.; Butryn, A.; Brem, J.; Gul, S.; Fuller, F. D.; Kim, I.-S.; Cheah, M. H.; Fransson, T.; Bhowmick, A.; Young, I. D.; O'Riordan, L.; Brewster, A. S.; Pettinati, I.; Doyle, M.; Joti, Y.; Owada, S.; Tono, K.; Batyuk, A.; Hunter, M. S.; Alonso-Mori, R.; Bergmann, U.; Owen, R. L.; Sauter, N. K.; Claridge, T. D. W.; Robinson, C. V.; Yachandra, V. K.; Yano, J.; Kern, J. F.; Orville, A. M.; Schofield, C. J. X-Ray Free-Electron Laser Studies Reveal Correlated Motion during Isopenicillin *N* Synthase Catalysis. *Sci. Adv.* **2021**, *7*, No. eabh0250.
(27) Hancock, R. L.; Abboud, M. I.; Smart, T. J.; Flashman, E.; Kawamura, A.; Schofield, C. J.; Hopkinson, R. J. Lysine-241 Has a Role in Coupling 2OG Turnover with Substrate Oxidation During KDM4-Catalysed Histone Demethylation. *ChemBioChem* **2018**, *19*, 917−921.
(28) Ramanan, R.; Chaturvedi, S. S.; Lehnert, N.; Schofield, C. J.; Karabencheva-Christova, T. G.; Christov, C. Z. Catalysis by the JmjC Histone Demethylase KDM4A Integrates Substrate Dynamics, Correlated Motions and Molecular Orbital Control. *Chem. Sci.* **2020**, *11*, 9950−9961.
(29) Waheed, S. O.; Chaturvedi, S. S.; Karabencheva-Christova, T. G.; Christov, C. Z. Catalytic Mechanism of Human Ten-Eleven Translocation-2 (TET2) Enzyme: Effects of Conformational Changes, Electric Field, and Mutations. *ACS Catal.* **2021**, *11*, 3877−3890.
(30) Chaturvedi, S. S.; Ramanan, R.; Hu, J.; Hausinger, R. P.; Christov, C. Z. Atomic and Electronic Structure Determinants Distinguish between Ethylene Formation and L-Arginine Hydroxylation Reaction Mechanisms in the Ethylene-Forming Enzyme. *ACS Catal.* **2021**, *11*, 1578−1592.
(31) Light, K. M.; Hangasky, J. A.; Knapp, M. J.; Solomon, E. I. Spectroscopic Studies of the Mononuclear Non-Heme Fe^{II} Enzyme FIH: Second-Sphere Contributions to Reactivity. *J. Am. Chem. Soc.* **2013**, *135*, 9665−9674.
(32) Goldberg, N. W.; Knight, A. M.; Zhang, R. K.; Arnold, F. H. Nitrene Transfer Catalyzed by a Non-Heme Iron Enzyme and Enhanced by Non-Native Small-Molecule Ligands. *J. Am. Chem. Soc.* **2019**, *141*, 19585−19588.
(33) Miller, G. P.; Wahnon, D. C.; Benkovic, S. J. Interloop Contacts Modulate Ligand Cycling during Catalysis by *Escherichia Coli* Dihydrofolate Reductase†. *Biochemistry* **2001**, *40*, 867−875.
(34) Arnold, F. H. Directed Evolution: Bringing New Chemistry to Life. *Angew. Chem., Int. Ed.* **2018**, *57*, 4143−4148.
(35) Leaver-Fay, A.; Tyka, M.; Lewis, S. M.; Lange, O. F.; Thompson, J.; Jacak, R.; Kaufman, K. W.; Renfrew, P. D.; Smith, C. A.; Sheffler, W.; Davis, I. W.; Cooper, S.; Treuille, A.; Mandell, D. J.; Richter, F.; Ban, Y.-E. A.; Fleishman, S. J.; Corn, J. E.; Kim, D. E.; Lyskov, S.; Berrondo, M.; Mentzer, S.; Popović, Z.; Havranek, J. J.; Karanicolas, J.; Das, R.; Meiler, J.; Kortemme, T.; Gray, J. J.; Kuhlman, B.; Baker, D.; Bradley, P.Rosetta3. In *Computer Methods, Part C*; Johnson, M.; Brand, L., Eds.; Methods in Enzymology; Elsevier, 2011; Vol. *487*, pp 545−574.
(36) Jiang, L.; Althoff, E. A.; Clemente, F. R.; Doyle, L.; Rothlisberger, D.; Zanghellini, A.; Gallaher, J. L.; Betker, J. L.; Tanaka, F.; Barbas, C. F.; Hilvert, D.; Houk, K. N.; Stoddard, B. L.; Baker, D. De Novo Computational Design of Retro-Aldol Enzymes. *Science* **2008**, *319*, 1387−1391.
(37) Siegel, J. B.; Zanghellini, A.; Lovick, H. M.; Kiss, G.; Lambert, A. R.; St Clair, J. L.; Gallaher, J. L.; Hilvert, D.; Gelb, M. H.; Stoddard, B. L.; Houk, K. N.; Michael, F. E.; Baker, D. Computational Design of an Enzyme Catalyst for a Stereoselective Bimolecular Diels-Alder Reaction. *Science* **2010**, *329*, 309−313.
(38) Romero-Rivera, A.; Garcia-Borràs, M.; Osuna, S. Role of Conformational Dynamics in the Evolution of Retro-Aldolase Activity. *ACS Catal.* **2017**, *7*, 8524−8532.
(39) Crean, R. M.; Biler, M.; van der Kamp, M. W.; Hengge, A. C.; Kamerlin, S. C. L. Loop Dynamics and Enzyme Catalysis in Protein Tyrosine Phosphatases. *J. Am. Chem. Soc.* **2021**, *143*, 3830−3845.
(40) Dodani, S. C.; Kiss, G.; Cahn, J. K. B.; Su, Y.; Pande, V. S.; Arnold, F. H. Discovery of a Regioselectivity Switch in Nitrating P450s Guided by Molecular Dynamics Simulations and Markov Models. *Nat. Chem.* **2016**, *8*, 419−425.
(41) Rabe, P.; Beale, J. H.; Butryn, A.; Aller, P.; Dirr, A.; Lang, P. A.; Axford, D. N.; Carr, S. B.; Leissing, T. M.; McDonough, M. A.; Davy, B.; Ebrahim, A.; Orlans, J.; Storm, S. L. S.; Orville, A. M.; Schofield, C. J.; Owen, R. L. Anaerobic Fixed-Target Serial Crystallography. *IUCrJ* **2020**, *7*, 901−912.

https://doi.org/10.1021/jacsau.2c00345
JACS Au 2022, 2, 2169−2186

(42) Ali, H. S.; Visser, S. P. Electrostatic Perturbations in the Substrate-Binding Pocket of Taurine/A-Ketoglutarate Dioxygenase Determine Its Selectivity. *Chem.—Eur. J.* **2022**, *28*, No. e202104167.
(43) Stuyver, T.; Ramanan, R.; Mallick, D.; Shaik, S. Oriented (Local) Electric Fields Drive the Millionfold Enhancement of the H-Abstraction Catalysis Observed for Synthetic Metalloenzyme Analogues. *Angew. Chem., Int. Ed.* **2020**, *59*, 7915−7920.
(44) de Visser, S. P.; Mukherjee, G.; Ali, H. S.; Sastri, C. V. Local Charge Distributions, Electric Dipole Moments, and Local Electric Fields Influence Reactivity Patterns and Guide Regioselectivities in α-Ketoglutarate-Dependent Non-Heme Iron Dioxygenases. *Acc. Chem. Res.* **2022**, *55*, 65−74.
(45) Chaturvedi, S. S.; Ramanan, R.; Lehnert, N.; Schofield, C. J.; Karabencheva-Christova, T. G.; Christov, C. Z. Catalysis by the Non-Heme Iron(II) Histone Demethylase PHF8 Involves Iron Center Rearrangement and Conformational Modulation of Substrate Orientation. *ACS Catal.* **2020**, *10*, 1195−1209.
(46) Horton, J. R.; Upadhyay, A. K.; Qi, H. H.; Zhang, X.; Shi, Y.; Cheng, X. Enzymatic and Structural Insights for Substrate Specificity of a Family of Jumonji Histone Lysine Demethylases. *Nat. Struct. Mol. Biol.* **2010**, *17*, 38−43.
(47) Yue, W. W.; Hozjan, V.; Ge, W.; Loenarz, C.; Cooper, C. D. O.; Schofield, C. J.; Kavanagh, K. L.; Oppermann, U.; McDonough, M. A. Crystal Structure of the PHF8 Jumonji Domain, an N^{ϵ}-Methyl Lysine Demethylase. *FEBS Lett.* **2010**, *584*, 825−830.
(48) Loenarz, C.; Ge, W.; Coleman, M. L.; Rose, N. R.; Cooper, C. D. O.; Klose, R. J.; Ratcliffe, P. J.; Schofield, C. J. PHF8, a Gene Associated with Cleft Lip/Palate and Mental Retardation, Encodes for an Nε-Dimethyl Lysine Demethylase. *Hum. Mol. Genet.* **2010**, *19*, 217−222.
(49) Björkman, M.; Östling, P.; Härmä, V.; Virtanen, J.; Mpindi, J.-P.; Rantala, J.; Mirtti, T.; Vesterinen, T.; Lundin, M.; Sankila, A.; Rannikko, A.; Kaivanto, E.; Kohonen, P.; Kallioniemi, O.; Nees, M. Systematic Knockdown of Epigenetic Enzymes Identifies a Novel Histone Demethylase PHF8 Overexpressed in Prostate Cancer with an Impact on Cell Proliferation, Migration and Invasion. *Oncogene* **2012**, *31*, 3444−3456.
(50) Wang, Q.; Ma, S.; Song, N.; Li, X.; Liu, L.; Yang, S.; Ding, X.; Shan, L.; Zhou, X.; Su, D.; Wang, Y.; Zhang, Q.; Liu, X.; Yu, N.; Zhang, K.; Shang, Y.; Yao, Z.; Shi, L. Stabilization of Histone Demethylase PHF8 by USP7 Promotes Breast Carcinogenesis. *J. Clin. Invest.* **2016**, *126*, 2205−2220.
(51) Zhu, G.; Liu, L.; She, L.; Tan, H.; Wei, M.; Chen, C.; Su, Z.; Huang, D.; Tian, Y.; Qiu, Y.; Liu, Y.; Zhang, X. Elevated Expression of Histone Demethylase PHF8 Associates with Adverse Prognosis in Patients of Laryngeal and Hypopharyngeal Squamous Cell Carcinoma. *Epigenomics* **2015**, *7*, 143−153.
(52) Chaturvedi, S. S.; Ramanan, R.; Waheed, S. O.; Ainsley, J.; Evison, M.; Ames, J. M.; Schofield, C. J.; Karabencheva-Christova, T. G.; Christov, C. Z. Conformational Dynamics Underlies Different Functions of Human KDM7 Histone Demethylases. *Chem.—Eur. J.* **2019**, *25*, 5422−5426.
(53) Chaturvedi, S. S.; Ramanan, R.; Waheed, S. O.; Karabencheva-Christova, T. G.; Christov, C. Z.Structure-Function Relationships in KDM7 Histone Demethylases. In *Advances in Protein Chemistry and Structural Biology*; Elsevier, 2019; Vol. *117*, pp 113−125.
(54) Case, D. A.; Ben-Shalom, I. Y.; Brozell, S. R.; Cerutti, D. S.; Cheatham, T. E. I.; Cruzeiro, V. W. D.; Darden, T. A.; Duke, R. E.; Ghoreishi, D.; Gilson, M. K.; Gohlke, H.; Goetz, A. W.; Greene, D.; Harris, R.; Homeyer, N.; Huang, Y.; Izadi, S.; Kovalenko, A.; Kurtzman, T.; Lee, T. S.; LeGrand, S.; Li, P.; Lin, C.; Liu, J.; Luchko, T.; Luo, R.; Mermelstein, D. J.; Merz, K. M.; Miao, Y.; Monard, G.; Nguyen, C.; Nguyen, H.; Omelyan, I.; Onufriev, A.; Pan, F.; Qi, R.; Roe, D. R.; Roitberg, A.; Sagui, C.; Schott-Verdugo, S.; Shen, J.; Simmerling, C. L.; Smith, J.; Salomon-Ferrer, R.; Swails, J.; Walker, R. C.; Wang, J.; Wei, H.; Wolf, R. M.; Wu, X.; Xiao, L.; York, D. M.; Kollman, P. A.*AMBER*; University of California: San Francisco, 2018.
(55) Metz, S.; Kästner, J.; Sokol, A. A.; Keal, T. W.; Sherwood, P. ChemShell—a Modular Software Package for QM/MM Simulations. *WIREs Comput. Mol. Sci.* **2014**, *4*, 101−110.
(56) Ahlrichs, R.; Bär, M.; Häser, M.; Horn, H.; Kölmel, C. Electronic Structure Calculations on Workstation Computers: The Program System Turbomole. *Chem. Phys. Lett.* **1989**, *162*, 165−169.
(57) Smith, W.; Yong, C. W.; Rodger, P. M. DL_POLY: Application to Molecular Simulation. *Mol. Simul.* **2002**, *28*, 385−471.
(58) Graham, S. E.; Syeda, F.; Cisneros, G. A. Computational Prediction of Residues Involved in Fidelity Checking for DNA Synthesis in DNA Polymerase I. *Biochemistry* **2012**, *51*, 2569−2578.
(59) Cisneros, G. A.; Perera, L.; Schaaper, R. M.; Pedersen, L. C.; London, R. E.; Pedersen, L. G.; Darden, T. A. Reaction Mechanism of the ε Subunit of *E. coli* DNA Polymerase III: Insights into Active Site Metal Coordination and Catalytically Significant Residues. *J. Am. Chem. Soc.* **2009**, *131*, 1550−1556.
(60) Lewis, J. C. Beyond the Second Coordination Sphere: Engineering Dirhodium Artificial Metalloenzymes To Enable Protein Control of Transition Metal Catalysis. *Acc. Chem. Res.* **2019**, *52*, 576−584.
(61) Lee, J.; Goodey, N. M. Catalytic Contributions from Remote Regions of Enzyme Structure. *Chem. Rev.* **2011**, *111*, 7595−7624.
(62) Ramanan, R.; Waheed, S. O.; Schofield, C. J.; Christov, C. Z. What Is the Catalytic Mechanism of Enzymatic Histone N-Methyl Arginine Demethylation and Can It Be Influenced by an External Electric Field? *Chem.—Eur. J.* **2021**, *27*, 11827−11836.
(63) Waheed, S. O.; Ramanan, R.; Chaturvedi, S. S.; Lehnert, N.; Schofield, C. J.; Christov, C. Z.; Karabencheva-Christova, T. G. Role of Structural Dynamics in Selectivity and Mechanism of Non-Heme Fe(II) and 2-Oxoglutarate-Dependent Oxygenases Involved in DNA Repair. *ACS Cent. Sci.* **2020**, *6*, 795−814.
(64) Torabifard, H.; Cisneros, G. A. Insight into Wild-Type and T1372E TET2-Mediated 5hmC Oxidation Using *Ab Initio* QM/MM Calculations. *Chem. Sci.* **2018**, *9*, 8433−8445.
(65) Martí, S.; Roca, M.; Andrés, J.; Moliner, V.; Silla, E.; Tuñón, I.; Bertrán, J. Theoretical Insights in Enzyme Catalysis. *Chem. Soc. Rev.* **2004**, *33*, 98−107.
(66) Warshel, A.; Sharma, P. K.; Kato, M.; Xiang, Y.; Liu, H.; Olsson, M. H. M. Electrostatic Basis for Enzyme Catalysis. *Chem. Rev.* **2006**, *106*, 3210−3235.
(67) Shaik, S.; Ramanan, R.; Danovich, D.; Mandal, D. Structure and Reactivity/Selectivity Control by Oriented-External Electric Fields. *Chem. Soc. Rev.* **2018**, *47*, 5125−5145.
(68) Shaik, S.; Mandal, D.; Ramanan, R. Oriented Electric Fields as Future Smart Reagents in Chemistry. *Nat. Chem.* **2016**, *8*, 1091−1098.
(69) Stuyver, T.; Huang, J.; Mallick, D.; Danovich, D.; Shaik, S. TITAN: A Code for Modeling and Generating Electric Fields—Features and Applications to Enzymatic Reactivity. *J. Comput. Chem.* **2020**, *41*, 74−82.
(70) Usharani, D.; Janardanan, D.; Shaik, S. Does the TauD Enzyme Always Hydroxylate Alkanes, While an Analogous Synthetic Non-Heme Reagent Always Desaturates Them? *J. Am. Chem. Soc.* **2011**, *133*, 176−179.
(71) Fang, D.; Lord, R. L.; Cisneros, G. A. *Ab Initio* QM/MM Calculations Show an Intersystem Crossing in the Hydrogen Abstraction Step in Dealkylation Catalyzed by AlkB. *J. Phys. Chem. B* **2013**, *117*, 6410−6420.
(72) Alvarez-Barcia, S.; Kästner, J. Atom Tunneling in the Hydroxylation Process of Taurine/α-Ketoglutarate Dioxygenase Identified by Quantum Mechanics/Molecular Mechanics Simulations. *J. Phys. Chem. B* **2017**, *121*, 5347−5354.

NOTE ADDED AFTER ASAP PUBLICATION

This paper was published ASAP on August 18, 2022. As of September 15, 2022, the authors and the Editor have issued a correction for this article. The clinical term "X-linked mental retardation" in the Abstract, Introduction, and Results and

https://doi.org/10.1021/jacsau.2c00345
JACS Au 2022, 2, 2169−2186

Discussion was replaced with "X-linked intellectual disability" which was adapted as replacement clinical terminology by the APA's fifth edition of the Diagnostic and Statistical Manual of Mental Disorders (DSM-5).

https://doi.org/10.1021/jacsau.2c00345
JACS Au 2022, 2, 2169−2186